JASA ARTICLE

Observations of low-frequency, long-range acoustic propagation in the Philippine Sea and comparisons with mode transport theory

Tarun K. Chandrayadula,[1,a)] Sivaselvi Periyasamy,[1] John A. Colosi,[2] Peter F. Worcester,[3] Matthew A. Dzieciuch,[3] James A. Mercer,[4] and Rex K. Andrew[4]

[1]Department of Ocean Engineering, Indian Institute of Technology Madras, Adyar, Chennai 600036, India

[2]Department of Oceanography, Naval Postgraduate School, 1 University Circle, Monterey, California 93943, USA

[3]Scripps Institution of Oceanography, University of California San Diego, 9500 Gilman Drive, La Jolla, California 92093, USA

[4]Applied Physics Laboratory, University of Washington, Seattle, Washington 98105, USA

ABSTRACT:
The year-long Philippine Sea (2010–2011) experiment (PhilSea) was an extensive deep water acoustic propagation experiment in which there were six different sources transmitting to a water column spanning a vertical line array. The six sources were placed in an array with a radius of 330 km and transmitted at frequencies in the 200–300 Hz and 140–205 Hz bands. The PhilSea frequencies are higher than previous deep water experiments in the North Pacific for which modal analyses were performed. Further, the acoustic paths sample a two-dimensional area that is rich in internal tides, waves, and eddies. The PhilSea observations are, thus, a new opportunity to observe acoustic modal variability at higher frequencies than before and in an oceanographically dynamic region. This paper focuses on mode observations around the mid-water depths. The mode observations are used to compute narrowband statistics such as transmission loss and broadband statistics such as peak pulse intensity, travel time wander, time spreads, and scintillation indices. The observations are then compared with a new hybrid broadband transport theory. The model-data comparisons show excellent agreement for modes 1–10 and minor deviations for the rest. The discrepancies in the comparisons are related to the limitations of the hybrid model and oceanographic fluctuations other than internal waves. https://doi.org/10.1121/10.0000587

(Received 20 August 2019; revised 12 December 2019; accepted 17 December 2019; published online 7 February 2020)

[Editor: D. Benjamin Reeder] Pages: 877–897

I. INTRODUCTION

The Philippine Sea experiment PhilSea10 (2010–2011) is one of the most extensive deep-water ocean acoustic experiments conducted to date (Worcester *et al.*, 2013). Figure 1 shows the map of the experiment location. The six sources (T1–T6) placed in an array of radius 330 km transmitted signals to a water-column-spanning distributed vertical line array (DVLA). Comparing PhilSea10 to previous deep water experiments, the sources transmitted signals with bandwidths of 140–205 Hz and 200–300 Hz, which are higher frequencies than the previous experiments for which modal analyses were performed (Mercer *et al.*, 2009; Worcester *et al.*, 1999; Worcester and Spindel, 2005). In addition to that, while earlier experiments took place in the "benign" regions of the eastern North Pacific, the PhilSea10 site was oceanographically dynamic with tides, eddies, and internal wave effects (Colosi *et al.*, 2013b; Kerry *et al.*, 2013; Niwa and Hibiya, 2004; Qiu, 1999; Qiu and Chen, 2010). The oceanographic variations are expected to be anisotropic across the different PhilSea10 propagation paths. The PhilSea10 observations are, thus, a new opportunity to observe acoustic modal variability at a new set of frequencies and in an oceanographically dynamic region with significant lateral anisotropy. This paper focuses on observations of the energy that arrives last, "the finale." The observations include intensities, travel time variability, and time spreads.

The arrivals in the finale contain diffracted energy that is best described using the modes of the waveguide (Jensen *et al.*, 1994). This paper compares mode observations with scattering theory predictions. In order to estimate the modes, this paper spatially filters the receptions on the DVLA (Wage, 2000; Wage *et al.*, 2003). The mode filtering calculations show that the PhilSea10 array can adequately resolve modes 1–20. Mode statistics are estimated for the propagation paths from the six sources to the DVLA. To predict the mode statistics, this paper uses the scattering-physics-based transport theory (Colosi *et al.*, 2013a; Colosi and Morozov, 2009). Models for broadband statistics for the lowest modes have previously either used Monte-Carlo type simulation studies or empirical studies from experiments (Chandrayadula *et al.*, 2013b; Colosi and Flatte, 1996; Wage *et al.*, 2003). Work by Udovydchenkov *et al.* (2012) and Udovydchenkov and Brown (2008) uses the ray-theory-based action variable concept to predict the mode time

[a)]Electronic mail: tkchandr@iitm.ac.in

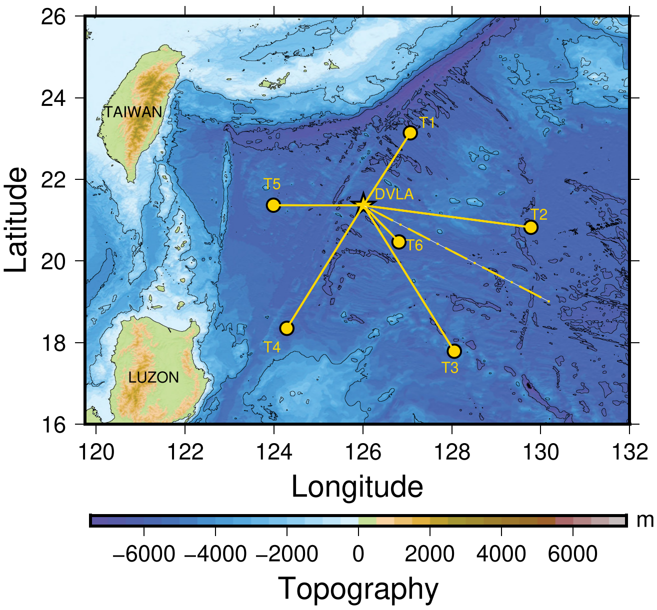

FIG. 1. (Color online) PhilSea 2010-2011 experiment (PhilSea10) location. The locations T1–T6 denote the source moorings. The DVLA receiver consisted of 149 hydrophones. For source ranges refer to Table I. The dashed-dotted line path between T2 and T3 indicates the ship locations along which CTD casts were made between May 14 and 22 (2010).

spreads. Udovydchenkov *et al.* (2012) suggested that the low mode time spreads varied in a non-uniform manner across range, with faster rates of variation predicted at short and long ranges than at the intermediate ranges. However, Udovydchenkov *et al.* (2012) did not provide a model that incorporates the mode scattering physics to predict the mode arrival structure. For mode statistics, transport theory has so far been successful in predicting narrowband scattering statistics (energies, time coherences, and cross-modal coherences) during the previous deep water experiments in the eastern North Pacific (Chandrayadula *et al.*, 2013a; Colosi *et al.*, 2013a). This work extends the approach to predict cross-frequency coherences to model mode time spreads, peak intensities, and travel-time wander. Modeling the broadband statistics via transport theory is, however, a computationally intensive operation. In order to overcome this challenge, the paper uses the hybrid approach (Raghukumar and Colosi, 2014). The statistics from the observations are then compared with the hybrid model predictions.

The rest of this paper is organized as follows. Section II describes the relevant details of the PhilSea10 experiment. Following that, Sec. III discusses the fundamentals of mode propagation in both range-independent and range-dependent environments. The discussion in Sec. III for range-dependent environments uses perturbation theory and transport theory. Sections IV and V then compare transport theory predictions with observations from PhilSea10. Finally, Sec. VI discusses the results and concludes the paper.

TABLE I. Source ranges and the respective bandwidths. The nominal bandwidths denote the differences between the maximum and minimum frequencies. The rms bandwidths are given by $\sqrt{[\int_f |H(f)|^2 f^2 df]/[\int_f |H(f)|^2 df]}$, where $H(f)$ is the frequency response of the sources (Fig. 2).

Source	Distance (km)	Carrier (Hz)	Nominal Bandwidth (Hz)	RMS Bandwidth (Hz)	Mean Source level (dB)
T1	224.844	250	100	22.0	188.6
T2	395.938	172.5	65	15.5	183.8
T3	450.131	275	100	21.1	181.8
T4	379.080	275	100	18.74	182.7
T5	210.055	255	100	28.5	183.9
T6	129.355	250	100	20.2	185.7

II. THE PHILIPPINE SEA EXPERIMENT (PHILSEA10)

The PhilSea10 experiment (2010–2011) was conducted from the end of April 2010 to the end of March 2011 (Worcester *et al.*, 2013) (Fig. 1). Sources T1–T6 transmitted 135-s long linear frequency modulated chirps to the DVLA. The sources were tunable organ type projectors (Morozov *et al.*, 2016). The array and the sources were moored in approximately 6000 m water depth. Table I shows the source-receiver ranges and the source frequencies. Source T6 is closest to the DVLA at 129 km, and T3 is the farthest at 450 km. Each of the sources has a non-uniform frequency response. The sources were calibrated following the experiment, at Seneca Lake (New York). Figure 2 shows the magnitude of the frequency responses. Five of the sources transmitted signals with bandwidths of 100 Hz that increased in frequency from about 200 to 300 Hz, while one (T2) transmitted signals that increased in frequency from 140 to 205 Hz. The calibrated phase responses were used to equalize the pulses. The transmissions from each source took place at 3-h intervals, every other day. While sources T1–T5 successfully transmitted for the entire duration of the experiment, T6 failed around the start of November 2010. The receiver array had 149 hydrophones that sampled at about 1 KHz. The hydrophones were located between depths of 150 and 5400 m. The hydrophones were localized with a long-baseline navigation system with an accuracy of less than a meter. The spacing between the hydrophones varied with depth. The shallowest and deepest hydrophones were spaced 40–60 m apart. The 76 hydrophones spanning the sound-channel axis (600–2100 m) were spaced 20 m apart. The hydrophones at the mid-water depths are sufficient to resolve the lowest modes. Figure 3 shows sample arrivals recorded during PhilSea10. The complexity of the arrival pattern increases with range.

Worcester *et al.* (2013) summarizes the general oceanography of the experiment site. The region is dynamic with eddies, internal waves, and multiple sites at which internal tides are generated (Colosi *et al.*, 2013b; Kerry *et al.*, 2013; Niwa and Hibiya, 2004; Qiu, 1999; Qiu and Chen, 2010; Ramp *et al.*, 2017). Internal tides are generated when barotropic tidal flows encounter steep bathymetry. Niwa and Hibiya (2004) and Kerry *et al.* (2013) use numerical

https://doi.org/10.1121/10.0000587

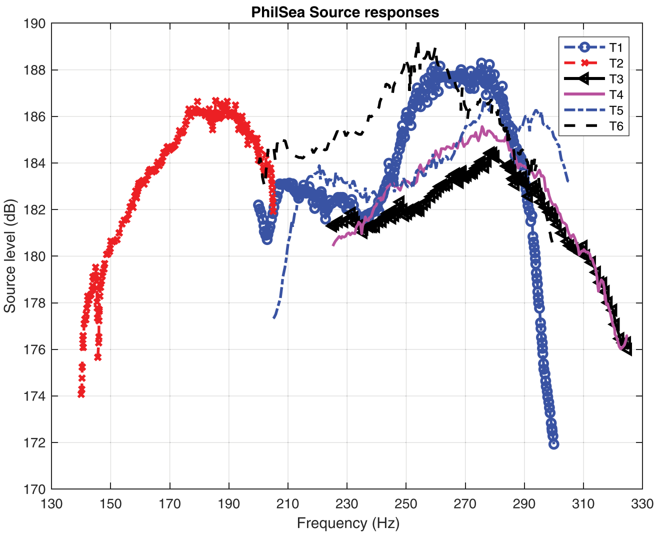

FIG. 2. (Color online) Philippine Sea source responses based on post-calibration tests performed at Seneca Lake, New York, during July 2011.

simulations and satellite data to determine the sites for internal tide generation in the Philippine Sea. The Luzon strait is the dominant source of internal tides in the PhilSea10 region. Colosi *et al.* (2013b) estimated the internal wave spectrum from the moored Conductivity Temperature Depth (CTD) sensors during the PhilSea 2009 pilot study. The estimated spectrum followed the Garett-Munk f^2 scaling in frequency with the root mean square internal wave displacement of 8.5 m.

Figure 4 shows the annual mean temperature and salinity profiles from the World Ocean Atlas (WOA) (Locarnini *et al.*, 2018a; Locarnini *et al.*, 2018b). The sound-speed profile was estimated from the temperature and salinities using the Del Grosso equation (Del Grosso, 1974).[1] The sound speed decreases to a minimum around 1000 m depth. The area around the minimum, the axis, is rather broad. The acoustic observations were complemented by environmental observations made during the experiment. The hydrophone modules at the receiver array contained thermistors that recorded the temperature every 20 min. Figure 4 also indicates the depths of CTD sensors colocated with the hydrophones. The CTD sensors were Sea Bird Microcats (*Sea Bird Electronics Inc. Washington, USA.*). Unfortunately, most of the sensors worked for only the first three months of the experiment because of battery issues that have since been fixed. Colosi *et al.* (2019) analyzed the moored CTD observations at the array. The observations were used to estimate the isopycnal displacement spectra at various depths. The spectrum showed an f^2 behavior in frequency, which is consistent with the GM spectrum. The depth scaling fit a reference root mean square (rms) displacement of 10 m. Apart from moored observations, ship CTD casts were made along a track that went from between T2 and T3 to the receiver array (Fig. 1). The casts were to a minimum depth of 1500 m, with every tenth cast full depth (5000–6000 m). The CTD casts were used to obtain a mean T–S curve. The T–S curve and the temperature measurements were used to obtain sound-speed profiles for use in mode filtering (Appendix).

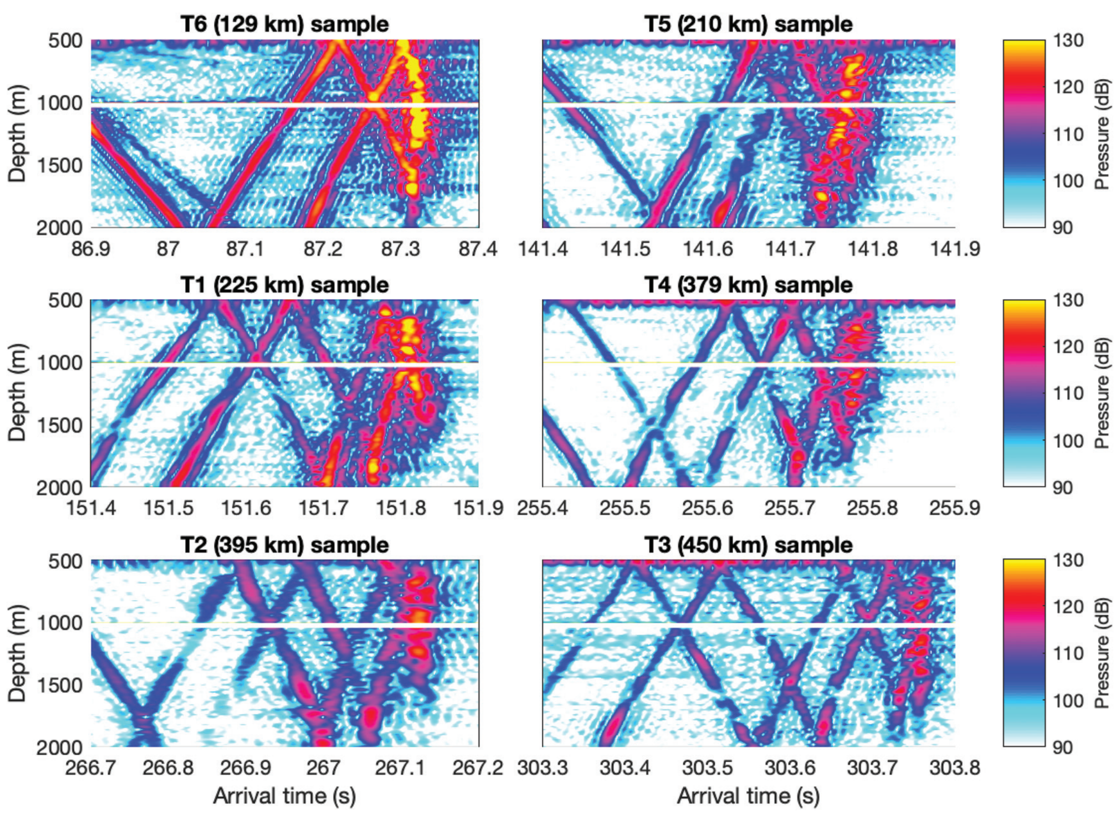

FIG. 3. (Color online) PhilSea 2010-2011 time fronts at ranges of 129 km to 450 km. The figures only display the finale of the arrival time fronts. The entire arrivals for transmissions from T6, T5, T1, T4, T2, and T3 last about 0.7, 1.2, 1.6, 2.3, 1.9, and 2.05 s, respectively. The transmissions occurred on 2 September 2010.

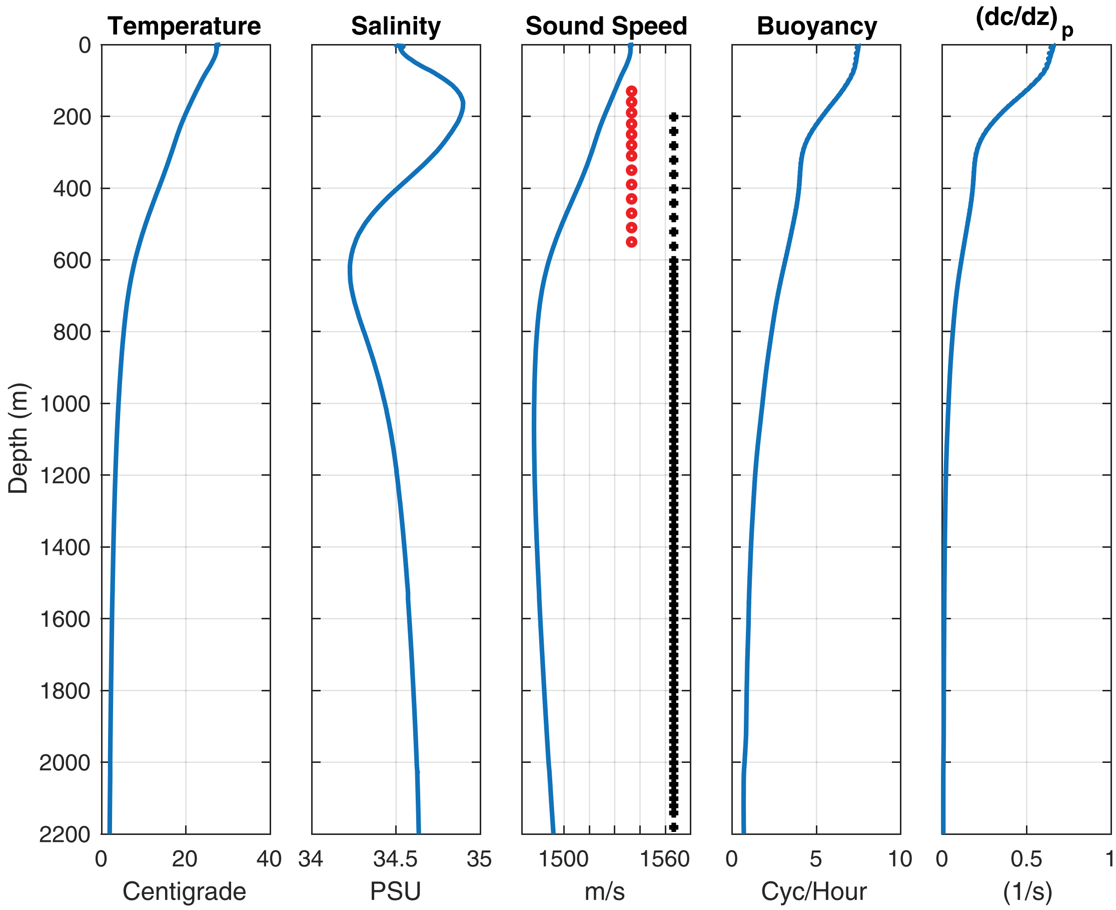

FIG. 4. (Color online) Mean temperature, salinity, sound-speed, buoyancy, and potential profiles for the Philippine Sea area. The mean profiles from the World Ocean Atlas (Locarnini *et al.*, 2018a; Locarnini *et al.*, 2018b) are an average from a total of 648 casts that were made between 16°N, and 123°–131°E. The panel for the SSP also indicates the depths of hydrophones and the CTD sensors at the array.

The mode spatial filter uses the mode shapes calculated at the array. The mode shapes $\psi_m(z)$ are the depth-dependent functions of the waveguide, which satisfy the equation (Jensen *et al.*, 1994)

$$\rho(z)\frac{d}{dz}\frac{1}{\rho(z)}\frac{d\psi_m(z)}{dz} + \left(k^2(z) - k_m^2\right)\psi_m(z) = 0, \tag{1}$$

where $\rho(z)$ is the density. The eigenvalues k_m are the wave numbers for each mode at a given angular frequency $\omega = 2\pi f$, and $k(z) = \omega/c(z)$. The mode shapes form an orthonormal basis set for the pressure field such that

$$p(r,z;\omega) = \sum_m \psi_m(r,z;\omega)a_m(r;\omega). \tag{2}$$

The complex weights $a_m(r)$ are the mode amplitudes. This paper uses Kraken numerical software to calculate the mode shapes and the wave numbers for a given SSP and frequency (Porter, 2001). Figure 5 shows the mode shapes calculated for the WOA SSP (Fig. 4). While the lowest modes span the sound-channel axis, the high modes (such as 50 and 100) describe the deep and shallow parts of the pressure field. The modes were processed using the broadband mode processing framework to spatially filter the receptions at the mid-water hydrophones (Wage, 2000; Wage *et al.*, 2003). The Appendix gives details on the mode processing, the mode beampatterns, and the handling of mismatch issues. Due to array resolution limitations, this paper only uses modes 1–20. Figure 6 shows sample mode processing results for the time fronts in Fig. 3. The internal waves and internal tides are expected to cause intensity fluctuations, temporal dispersion, and travel-time wander. This paper uses the mode observations (such as Fig. 6) to compute the statistics.

III. MODE PROPAGATION IN THE OCEAN

This section consists of two parts. This first discusses mode propagation in a range-independent background environment. The second discusses mode propagation in a range-dependent environment in which the background SSP varies due to oceanographic effects such as internal waves, internal tides, and the ocean mesoscale.

A. Acoustic predictions using a range-independent SSP

In a range-independent environment, the mode amplitudes are given by

$$a_m(r) = \psi_m(0,z_s)\frac{e^{ik_m r}}{\sqrt{8\pi k_m r}}. \tag{3}$$

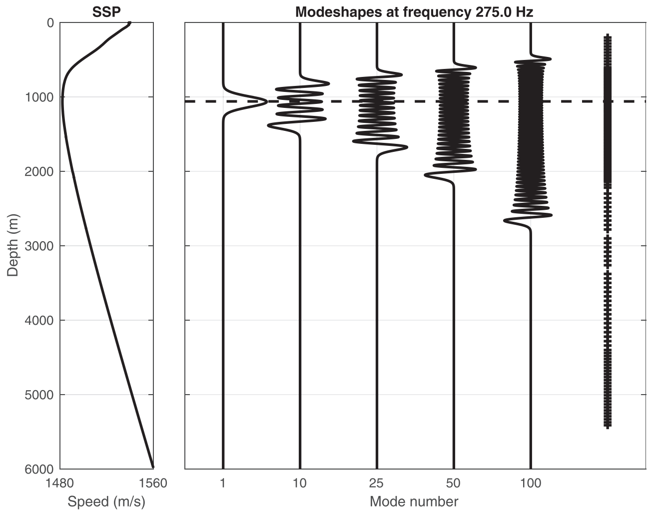

FIG. 5. Mode shapes for the PhilSea SSP (Fig. 4). The figure also indicates the depths of the receiver DVLA hydrophones and the approximate depth of the PhilSea sources (1050 m).

The mode amplitudes in a range-independent environment thus depend on the amplitude of the mode shape at the source depth ($\psi_m(0, z_s)$) and decrease with range due to cylindrical spreading. The wave numbers vary as a function of frequency. The calculations for the wave number versus frequency curves can be used to estimate dispersion curves from which the group velocities can be predicted. Figure 7 shows the travel-time predictions for the Philippine Sea ranges and frequencies (Table I). Sources T1, T3, T4, T5, and T6 occupy the same frequency band (200–300 Hz), and hence show similar dispersion. The lowest modes (1–10) suffer little frequency dispersion and arrive almost on top of each other. Source T2, which transmitted in a different frequency band (140–205 Hz), has dispersion predictions much different from the rest of the sources.

The differences in the amount of dispersion are due to the variability of the mode shapes across frequency. The mode shapes that satisfy Eq. (1) vary as a function of frequency (ω). While the number of oscillations for each mode number does not vary across frequency, the depth spread of

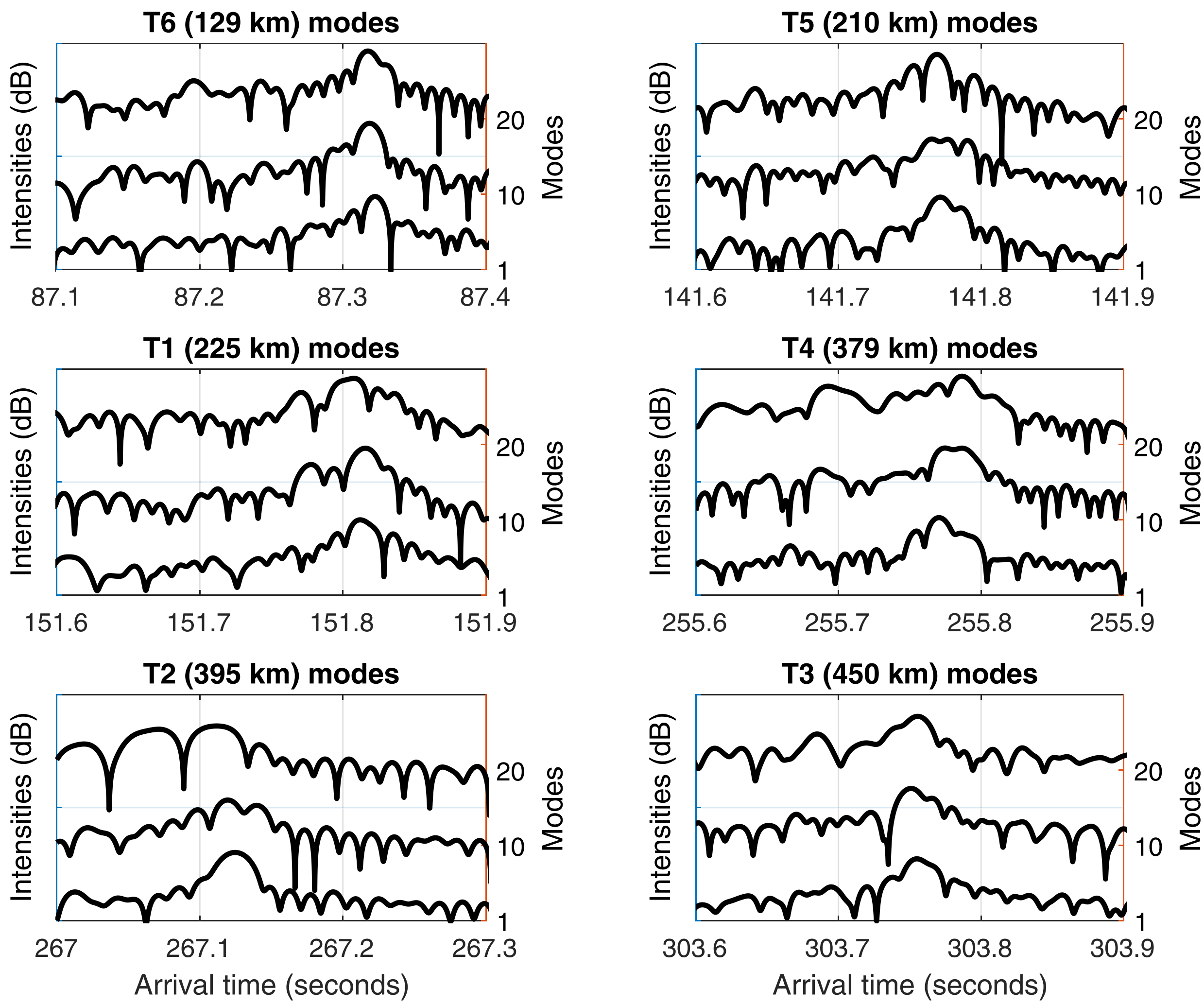

FIG. 6. (Color online) Arrivals for modes 1, 10, and 20 for transmissions from sources T1 to T6 (Fig. 3). The approximate peak intensity levels for the mode pulses are between 105 and 115 dB.

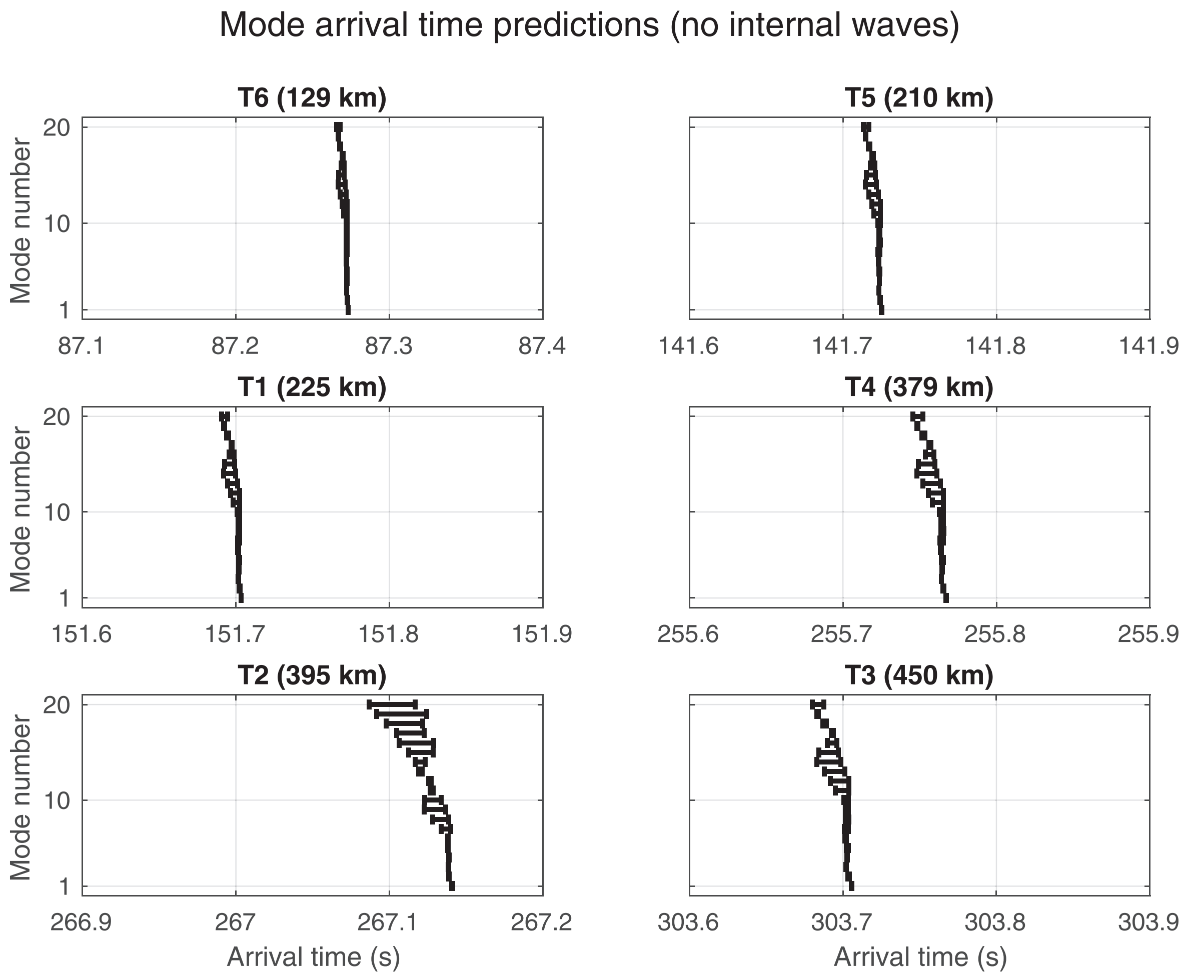

FIG. 7. Mode travel-time predictions for the PhilSea10 source ranges. The horizontal bars represent the minimum and maximum modal travel times for the signal bandwidths.

the mode shape changes. The depth extent can be quantified by a metric called the "turning depth." The terminology, actually borrowed from ray theory, indicates the minimum and maximum depths at which the oscillatory component of the mode shape $(k^2 - k_m^2)$ goes to zero. Figure 8 shows the turning depths for modes 1–20 for two different frequency bands. The frequency band 200–300 Hz is relevant for sources T1, T3, T4, T5, and T6, and the 140–205 Hz band pertains to the T2 source. For both frequency bands, the high modes show a greater spread in depth than the low modes. The 140–205 Hz band shows a greater spread in turning depths than the 200–300 Hz band. In addition to indicating the depth spreads, the turning depths are also where the modes are the most sensitive to sound-speed perturbations (travel-time sensitivity kernels described below). For the 200–300 Hz band (consistent with Fig. 8), the lowest mode 1 is the most sensitive to sound speed perturbation at the turning depths of 1000 and 1750 m, and mode 20 is most sensitive at 650–750 m and 1600–1775 m. Similar comparisons can be made for the 140–205 Hz band (Fig. 8). The larger spread of turning depths for the 140–205 Hz band suggests that these modes potentially become more decorrelated across frequency.

While mode theory is essentially a narrowband concept, the mode amplitudes at different frequencies can be combined to synthesize a mode time series. This leads to the idea of the "mode pulse." Udovydchenkov *et al.* (2012), Udovydchenkov and Brown (2008), and Chandrayadula *et al.* (2013b) discuss the mode pulse. The mode pulse $\alpha_m(r,t)$ at range r is given by a Fourier integral across the respective narrowband mode amplitudes,

$$\alpha_m(r,t) = \left| \frac{1}{2\pi} \int_{\omega} a_m(r,\omega) e^{i\omega t} d\omega \right|. \quad (4)$$

The intensity of the mode pulse is given by $\langle |\alpha_m(r,t)|^2 \rangle$. Figure 9 shows the intensity of the simulated mode pulses for the PhilSea10 ranges. The simulations used mode amplitudes calculated from the mode shapes based on the SSP in Fig. 4. The mode amplitudes were multiplied with the calibrated source frequency magnitude responses (Fig. 2) to make the simulations close to the data. In order to highlight the distribution of energy across mode number and cancel range scaling, the intensities were normalized with the sum of the mode (1–20) intensities. For the case that the intensities are equal across modes, the normalized intensities will

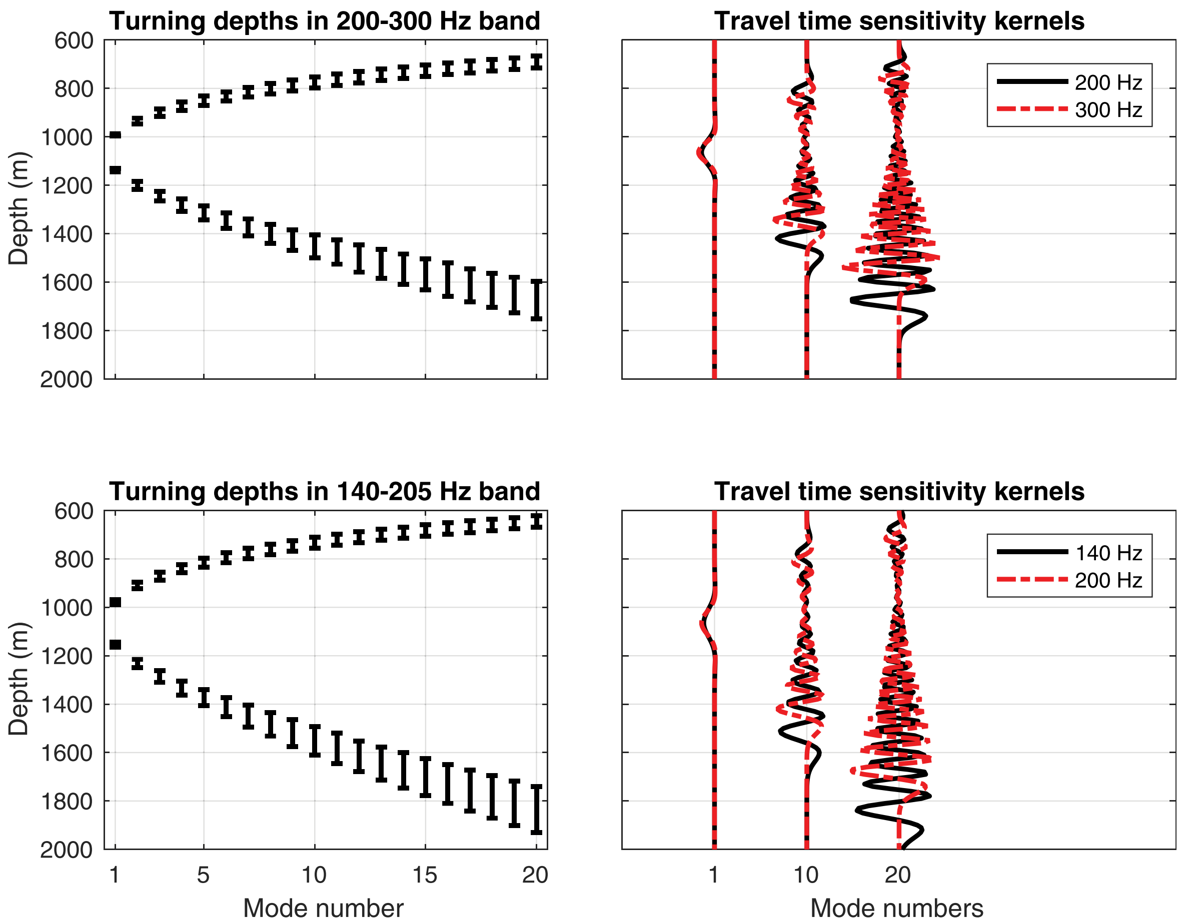

FIG. 8. (Color online) Plot of mode turning depths and the travel-time sensitivity kernels for two different frequency bands. The vertical bars represent the minimum and maximum values of the turning depths for the respective bandwidths. The turning depths were calculated from the mode wave number predictions for the WOA SSP in Fig. 5.

equal 0 dB. The mode peak intensities, however, show an alternating pattern of high and low amplitudes due to the different source excitation amplitudes for the respective mode number. Regarding the temporal spreads of the modes, note that the spreads are a sum of the inverse of bandwidth (Table I) and the dispersive time spread for the respective mode number (Fig. 7). In the absence of internal waves, the mode pulses in Fig. 9 show time spreads of around 10 ms for the sources T1, T3, T4, T5, and T6, and around 30 ms for source T2. The larger time spreads for T2 are due to the narrower bandwidth of the T2 source (65 Hz) in comparison to the other sources (100 Hz).

B. Mode propagation in the range-dependent ocean: Effects of the ocean mesoscale, internal tides, and internal waves

In a realistic long-range ocean environment, the sound-speed profile varies as a function of range, which causes the mode shapes and wave numbers to change. Equation (3) and the associated predictions in Figs. 7 and 9 that use range-independent mode calculations are thus inadequate to describe propagation in a range-varying ocean. For PhilSea10 experiment configuration and ranges, there are two types of relevant sound-speed perturbations across range and depth. The first is due to internal tides and the ocean mesoscale. The second type of sound-speed perturbation is due to small-scale effects caused by internal waves. This section uses different approaches to deal with each. For the mesoscale and internal tide, this section uses a perturbation theory model. For internal-wave perturbations, this section uses transport theory.

1. Travel time fluctuations due to internal tides and ocean mesoscale: Perturbation theory

The internal tides and ocean mesoscale, which have horizontal scales on the order of more than 10 s of kilometers, cause travel time perturbations due to a net change in the average sound speed. A first-order perturbation model by Shang (1989) specifies the travel time perturbation $\Delta\tau_m$ at a frequency ω as

$$\Delta\tau_m = \int_z\int_r \Delta c(r,z)\xi_m(z;\omega)drdz. \tag{5}$$

Equation (5) expresses the mode travel-time perturbation as a double integral across depth and range. The depth-dependent function $\xi_m(z)$ is called the mode travel-time sensitivity

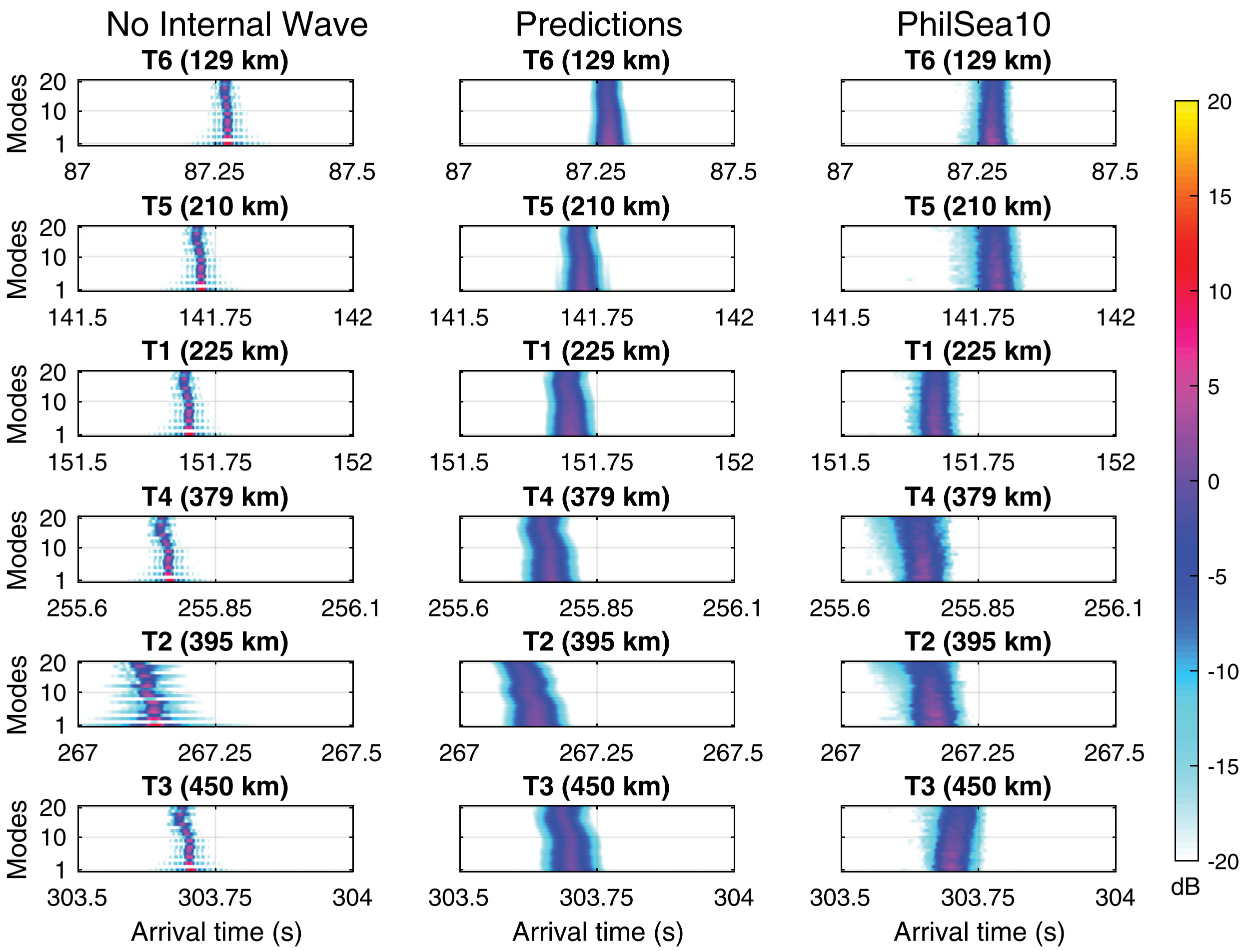

FIG. 9. (Color online) Intensity calculations for no-internal-wave case, transport theory predictions, and PhilSea10 observations. The mode (1–20) pulses from the observations show the average for the month of October 2010 (a total of 120 pulses for each mode). The intensities are normalized by scaling with respect to the total intensities of modes 1–20. A scaled-intensity level of 0 dB is equivalent to equal intensities for all the modes in the plot.

kernel (TSK). The expression for the mode TSK (Shang, 1989) is

$$\xi_m(z;\omega) = -\frac{R}{k_m}\frac{\left[\left(2\omega - \frac{v_{pm}}{v_{gm}}\omega\right)|\psi_m(z;\omega)|^2 + \omega^2\frac{\partial}{\partial\omega}|\psi_m(z;\omega)|^2\right]}{(c(z))^3}, \quad (6)$$

where v_{pm} is the mode phase velocity, and v_{gm} is the group velocity at ω. Figure 8 shows the mode (1, 10, and 20). TSKs calculated for the lowest and highest frequencies for two different bands (140–205 Hz and 200–300 Hz). The TSKs for the other modes lie between 1, 10, and 20. The mode TSKs are concentrated around the respective turning depths. The TSKs also show an asymmetry in depth weighting. Modes 1, 10, and 20 are more sensitive to perturbations at their lower turning depths than at their upper ones. The turning depths in Fig. 8 suggest that the lowest modes, such as mode 1, are sensitive to sound-speed perturbations around 1000 m and the higher modes are sensitive at depths greater than 1500 m.

The range scaling of the travel-time fluctuations depends on the correlation length scales and the directionality of the sound-speed perturbations. For sound-speed perturbations that have an incident azimuthal angle of θ and a wavelength of λ_{tide}, the travel time wander is proportional to the (unit-normalized) range integral $v(\theta,\lambda) = |(1/R)\int_0^R e^{j(2\pi/\lambda_{tide})\cos(\theta)r}dr|$ (Dushaw, 2003). The range integral is given by

$$v(\theta,\lambda_{tide}) = \frac{\sin\left[\frac{\pi R}{\lambda_{tide}}\cos(\theta)\right]}{\left(\frac{\pi R}{\lambda_{tide}}\right)\cos(\theta)}. \quad (7)$$

Internal tides occur at diurnal, semidiurnal, and other higher harmonic frequencies. In the PhilSea10 area, λ_{tide} for mode 1 internal tides at the diurnal and semi-diurnal frequencies are 410 and 165 km, respectively. Sound-speed perturbations due to internal tides can be highly directional. For tides that have their phase fronts parallel to the acoustic path, the travel time wander is a maximum, and for others, the travel-time wander is the average across several wavelengths. For the case that the wavelength of the perturbation is much smaller than the acoustic path length $R > \lambda_{tide}$ and $\theta \approx 0$, the tide-induced wander is minimal. For sound-speed perturbations that do not have a specific direction but are rather described by an overall wide-sense-stationary process in range, the travel time fluctuations follow a $\sqrt{R}$ dependence. The $\sqrt{R}$ dependence potentially holds true for a region with multiple internal tides and for mesoscale range perturbations.

2. Effects of internal waves on mode pulses: Hybrid transport theory

Acoustic scattering by internal waves is due to their small-scale structure. The internal waves have correlation scales of meters to a few kilometers in the horizontal. The scales are smaller in the vertical. The frequencies are between the Coriolis and Brunt-Vaisala frequencies. The internal-wave-induced sound-speed perturbations are best described using stochastic models (Colosi and Brown, 1998; Garrett and Munk, 1972, 1975), and thus there are no deterministic expressions for mode energies (narrowband), mode pulse intensity, and travel time variability. However, it can broadly be said that internal waves cause three types of effects on the modes. The first is time wander, the second is mode coupling in which modes exchange energies (Dozier and Tappert, 1978a,b), and the third is additional dispersive time spreads in the mode pulses due to coupling. Udovydchenkov *et al.* (2012) and Udovydchenkov and Brown (2008) used simulations to predict that time spreads due to dispersion scales R and due to internal wave scattering scales as $R^{3/2}$ for the high acoustic modes. Chandrayadula *et al.* (2013b) used a model based on empirical orthogonal functions of mode observations to build a statistical descriptor set for the mode pulses. This paper uses the scattering-physics-based transport theory equations to predict the variation of the narrowband energies ($\langle|a_n|^2\rangle$) and the cross-modal coherences $\langle a_n a_p^*\rangle$ with range. The transport theory equations for the mode problem were originally suggested in Dozier and Tappert (1978a,b), and then expanded by Colosi and Morozov (2009) and Colosi *et al.* (2013a). This approach is similar to diffusion equations that are well known in areas such as optics and heat transfer (Van Kampen, 2007). The equations are given by

$$\frac{d\langle a_n a_p^*\rangle}{dr} + i(k_p^* - k_n)\langle a_n a_p^*\rangle = \sum_{m=1}^{N}\sum_{q=1}^{N}\langle a_m a_q^*\rangle I_{mn,qp}^* + \langle a_q a_m^*\rangle I_{mp,qn}^* - \langle a_n a_q^*\rangle I_{mp,qm}^* - \langle a_q a_p^*\rangle I_{mn,qm}^*. \tag{8}$$

The I matrices are given by a wave number integral in range of the correlation of coupling matrices (Colosi, 2016; Colosi and Morozov, 2009). The correlation function for the coupling matrices depends on the acoustic mode shapes and parameters of the internal wave spectrum. Equation (8) can predict several mode statistics. The case $n=p$ yields mode energies $\langle|a_n|^2\rangle$ and for modes separated in time $\langle a_n(\tau)) a_n^*(\tau+\Delta\tau)\rangle$ predicts the time coherences (Colosi *et al.*, 2013a).

The transport theory method based on Eq. (8) can be used to model the broadband statistics of the mode pulse. Refer to Colosi (2016) for an initial treatment of the subject. Predicting the mode pulse statistics by a straightforward application of transport theory is, however, computationally tedious. The full broadband transport theory approach involves solving Eq. (8) for all the cross-combinations of n, p, ω_1, and ω_2. To get an idea of the computational complexity, note that while mode energy predictions for N modes require the solution of N^2 equations, cross-modal-cross-frequency calculations entail $O(N^4)$. Colosi (2016) uses an adiabatic approximation to obtain broadband coherences. The adiabatic approach accounts for the phase perturbations due to internal wave effects but excludes the cross-modal coupling in the energy calculations. The simulations in Colosi (2016) show that the adiabatic approximation to phase works well as long as the modes at the respective frequencies share the same turning depths. The success of the adiabatic phase approximation thus depends on the dispersion induced by the sound-speed profile. The adiabatic phase approximation, however, does not account for the energy transfer or decay that is important to describe the low mode arrivals. To include the cross-modal coupling and yet not suffer from a huge computational complexity, this paper will use the hybrid transport theory approach (Raghukumar and Colosi, 2014). The hybrid approach uses a combination of mode energy predictions $\langle|a_n(\omega_1)|^2\rangle$ at each frequency and the adiabatic approximation for cross-frequency coherence. The hybrid transport theory approximation for cross-frequency correlations is given by

$$\langle a_n(\omega_1)a_n^*(\omega_2)\rangle = \left\langle\sqrt{\langle|a_n(\omega_1)|^2\rangle\langle|a_n(\omega_2)|^2\rangle}e^{i(k_n(\omega_1)-k_n^*(\omega_2))r}e^{-\Theta(\omega_1,\omega_2)}\right\rangle. \tag{9}$$

The mode energies $\langle|a_n(\omega_1)|^2\rangle$, $\langle|a_n(\omega_2)|^2\rangle$ come from the narrowband transport theory [$O(N^2)$ calculations]. The phase structure function Θ is given by

$$\Theta(\omega_1,\omega_2)(R) = (I_{nn,nn}(\omega_1) + I_{nn,nn}(\omega_2) - 2I_{nn,nn}(\omega_1,\omega_2))R. \tag{10}$$

The phase structure function term accounts for the loss of coherence caused by time-wander. The approximation, however, discounts the loss of phase coherence due to mode coupling. The variance of the time wander at a frequency ω_0 is given by

$$\tau_n(\omega_0)^2 = \frac{1}{\omega_0^2}\frac{4N_0BR}{\pi^2 f_{Coriolis}}\sum_{j=1}^{J}\frac{H(j)}{j}G_{nn0}^2(j), \tag{11}$$

where $f_{Coriolis}$ is the Coriolis frequency, $H(j)$ is the variance of the internal wave modes (j), and G_{nn} is the integral of the

$\psi_n(z)$ shape across the Wentzel-Kramers-Brillouin (WKB) internal wave modes (Colosi, 2016; Colosi and Morozov, 2009). Thus, the travel-time wander $\sqrt{\langle \tau_n(\omega_0)^2 \rangle}$ is expected to follow a $\sqrt{R}$ dependence. This paper uses Eqs. (9) and (11) to predict the following statistics. The first statistic is the intensity of the mode pulse. The intensity ($\langle |\alpha_m(r,t)|^2 \rangle$) is predicted using a double Fourier integral given by

$$\langle |\alpha_m(t)|^2 \rangle = \frac{1}{2\pi}\int_{\omega_1} \frac{1}{2\pi}\int_{\omega_2} \langle a_m(\omega_1) a_m^*(\omega_2) \rangle \times e^{i(\omega_1-\omega_2)t} d\omega_1 d\omega_2. \tag{12}$$

The mode pulse will be used to predict the peak intensity and the pulse spread. The second statistic is the travel-time wander [Eq. (11)].

The PhilSea10 transport theory predictions were set up using the mode shapes calculated from the SSP and the buoyancy frequency profile in Fig. 4. For internal wave parameters, Colosi *et al.* (2019) used the CTD observations at the PhilSea10 array to estimate the appropriate rms internal wave displacement $\zeta_0 = 10$ m. This work uses $\zeta_0 = 10$ m, number of internal wave modes $J = 150$, reference sound speed $c_0 = 1480$ m/s, source depth $z_s = 1060$ m, reference buoyancy frequency $N_{ref} = 3$ cyc/h, and internal wave spectrum scaling parameter $j_* = 3$. Figure 10 shows the mode intensities $\langle |a_n|^2 \rangle$ (normalized with respect to the average of the mode 1–20 intensities) predicted using transport theory at a reference frequency of 250 Hz. The predictions show that there is a rapid redistribution of energies initially, and then the mode intensities seem to taper towards equilibrium. A similar calculation for the predicted cross-modal coherences $\langle a_n a_m^*(\omega) \rangle$ showed the modes rapidly decorrelating beyond a range of 50 km. Referring back to the mode pulse intensity predictions, Fig. 9 compares the broadband mode pulses with the no internal wave case. As for the no-internal-wave predictions, the mode intensities are normalized with respect to the mean (across modes 1–20). While the no-internal-wave mode case shows a wide spread of mode energies (from -10 to 3 dB), the hybrid prediction peak intensities hover from around -2 to $+2$ dB. Further, the spread of values in the predicted intensities gets smaller with an increase in range from 129 to 450 km. At the shortest range T6 (129 km), the predicted intensities vary from -2 to $+2$ dB. However, at the farthest range T3 (450 km), the predicted intensities vary by only about $\pm 0.5\,dB$.

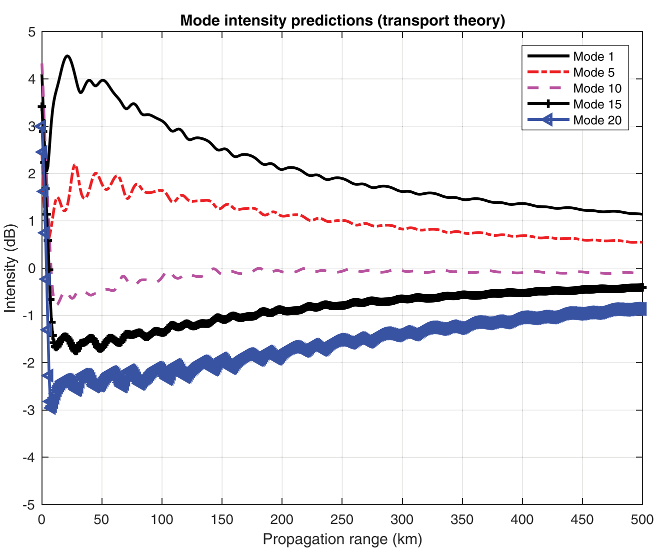

FIG. 10. (Color online) Intensity predictions across range from transport theory (Sec. III B). The intensities for each mode are normalized with respect to the sum of intensities across modes 1–20.

IV. COMPARISONS TO MODE OBSERVATIONS: TRAVEL TIME FLUCTUATIONS DUE TO MESOSCALE EFFECTS, INTERNAL TIDES, AND INTERNAL WAVES

The travel-time estimates use the centroids of the mode pulses (Wage *et al.*, 2003). The centroids are a relatively robust measure of arrival times in comparison to peak-picking. In order to estimate the centroids, a 0.5 s time window focusing on the main mode pulse was chosen. The centroid calculation used a threshold of 1/5 of the peak mode pulse amplitude in the window. Figure 11 shows the time series of the mode 1 centroid-based travel-time estimates for different source ranges. In order to track the main mode pulse, the centroid estimates use a cutoff 10 dB that is lower than the peak. The low-frequency variability is due to mesoscale effects that have time scales of several weeks. The fluctuations about the low-frequency variability are due to internal tides and internal waves. In order to segregate the fluctuations into the respective time scales, the following steps were done. The centroids were first low-pass filtered with a 3-day boxcar filter to measure the mesoscale variability. Figure 11 shows the estimated mesoscale trend for mode 1. The standard deviations of the mesoscale fluctuations (wander) for modes 1–20 were estimated for each month and averaged. Figure 12 in the left subplot shows the average wander (standard deviation) of the mesoscale variability for the different source ranges. For comparison among the different sources, the approximate median distance of 250 km was chosen as the reference. The right subplot shows the mesoscale wander scaled by $\left(\sqrt{250/R}\right)$. Source T4 shows the most wander, and source ranges T2 and T6 the least. Most of the source ranges (T2, T3, T4, T5, and T6) show a mode-number-dependent trend to the arrival time fluctuations. The high modes, such as 15–20, show less variability than the low modes (1–5).

For the internal tide, the mesoscale variability was first subtracted from the arrival-time series. The least squares (LS) fits were then performed using four diurnal and four semidiurnal constituents (M2, S2, N2, K2, O1, K1, P1, and Q1). Note that the PhilSea10 observations are undersampled (eight samples per 24 h, but only every other day). To ensure adequate frequency resolution (for PhilSea10 sampling), the LS fit was performed over two separate six-month blocks and then averaged. The first six-month block (for T1–T6) lasted from May to October 2010 and the second (for T1–T5) from November 2010 to March 2011. There were only the first six months for T6 and no second block due to a

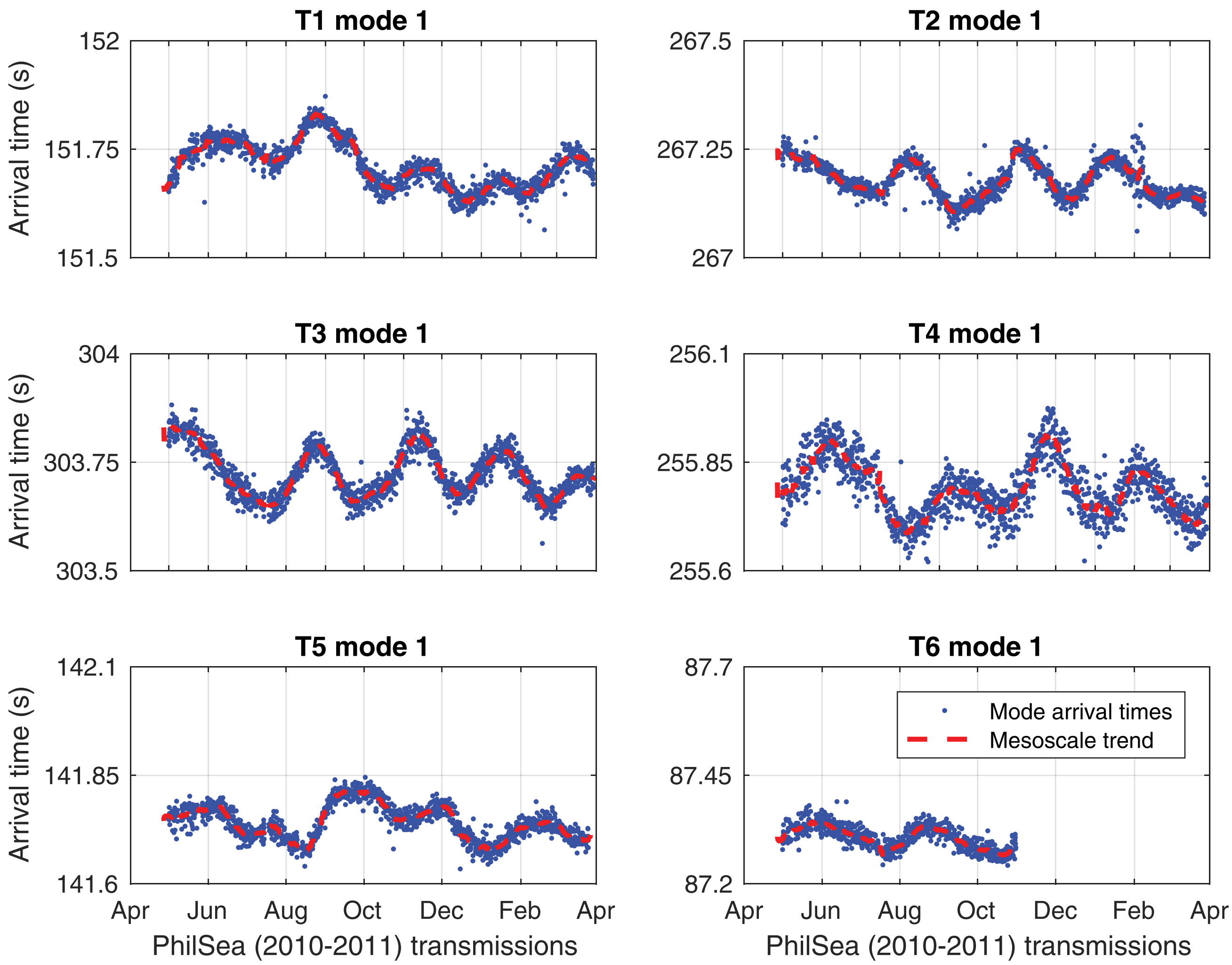

FIG. 11. (Color online) Mode 1 travel times for the PhilSea source ranges.

lack of data. The LS fits assumed a prior noise variance of 5 ms for the errors in the travel-time estimates. The error calculations for the LS fits showed a 0.3 ms error or less. Figure 13 compares the travel-time wander from the internal tide fits for the six different source ranges. Similar to the mesoscale, travel-time perturbations due to internal tides are expected to have a $\sqrt{R}$ scaling. The travel-time wanders scaled to $R_0 = 250$ km are shown in the right inset of Fig. 13. Source ranges T6 and T4 show the most wander, and T2 shows the lowest. It was, however, not feasible to predict travel-time fluctuations due to the internal tides in the Philippine Sea for comparisons with observations. Analyses of the CTD observations at the source locations (not discussed here) suggest a complicated internal tide structure. The power spectra show substantial variation in the dominant tidal frequencies between moorings and across different months. Tidal fits using sinusoids with a constant phase gave poor estimates with a high residual error. This is potentially due to multiple internal tide generation sites that change over time and to non-linear internal tides.

The internal tide fits were subtracted from the mesoscale-detrended travel times to estimate the residual contribution due to internal waves (Fig. 14). The travel-time wander due to internal waves is expected to follow a $\sqrt{R}$ dependence [see the discussion around Eq. (11)]. The estimates scaled to $R_0 = 250$ km are from 10 to 16 ms. The estimates show some variation with the source. It is, however, not clear if there is a meaningful difference between them. Figure 14 also shows the internal-wave-induced travel-time wander predictions [Eq. (11)]. The predicted wanders lie between a maximum of 10 ms at T6 and 20 ms at T3. The range dependence in the predictions was accounted for by scaling to a reference range $R_0 = 250$ km ($\sqrt{R_0/R}$ scaling). The scaled predictions have a wander around 14 ms for the lowest modes and around 12 ms for the highest modes. Considering the scaled estimates for the lowest modes (1–5), the travel-time wander for source ranges T1, T2, T4, T5, and T6 are within 1–2 ms of the predictions. The travel-time wander for source T3, is however, less than predicted, yet within a factor of 1.5. For modes greater than 10, the observations do not show the decrease in wander with an increase in mode number, which the hybrid predictions show.

Figure 15 compares the time spreads from the observations with the predictions. The predicted time spreads are

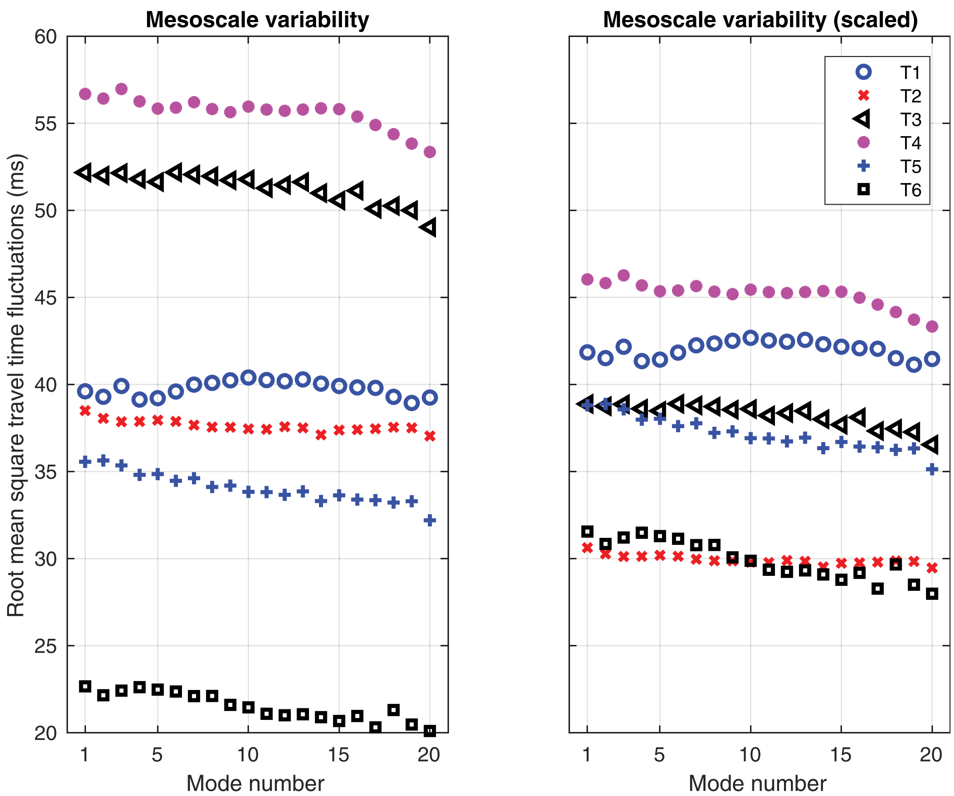

FIG. 12. (Color online) Average wander (standard deviation) of the mesoscale variability of the travel-time observations for modes 1–20 (left) and after scaling to a reference range of 250 km (right).

estimated from the pulse predictions in Fig. 9 using a cutoff 10 dB below the peak. The 10 dB cutoff was chosen for two reasons. First, the PhilSea10 pulses have their first sidelobes at 13 dB. The cutoff thus highlights the portion of the mode pulse where the bulk of the energy arrives. Second, for the higher modes such as 15–20, the signal-to-noise ratio (SNR) was only 12–13 dB at T6 due to the aliasing of the high modes. The 10 dB cutoff was uniform across mode number and source range. The hybrid mode predictions clearly show a wider temporal spread than the no-internal-wave

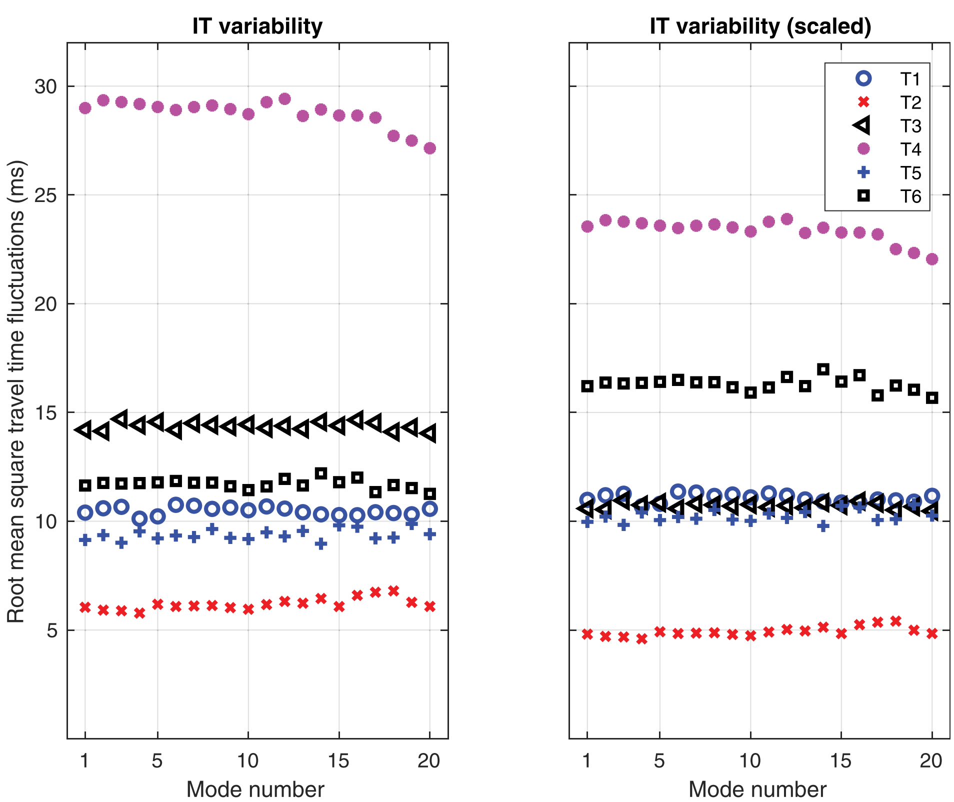

FIG. 13. (Color online) Same as Fig. 12, except for the travel-time variability due to internal tides from mode centroids.

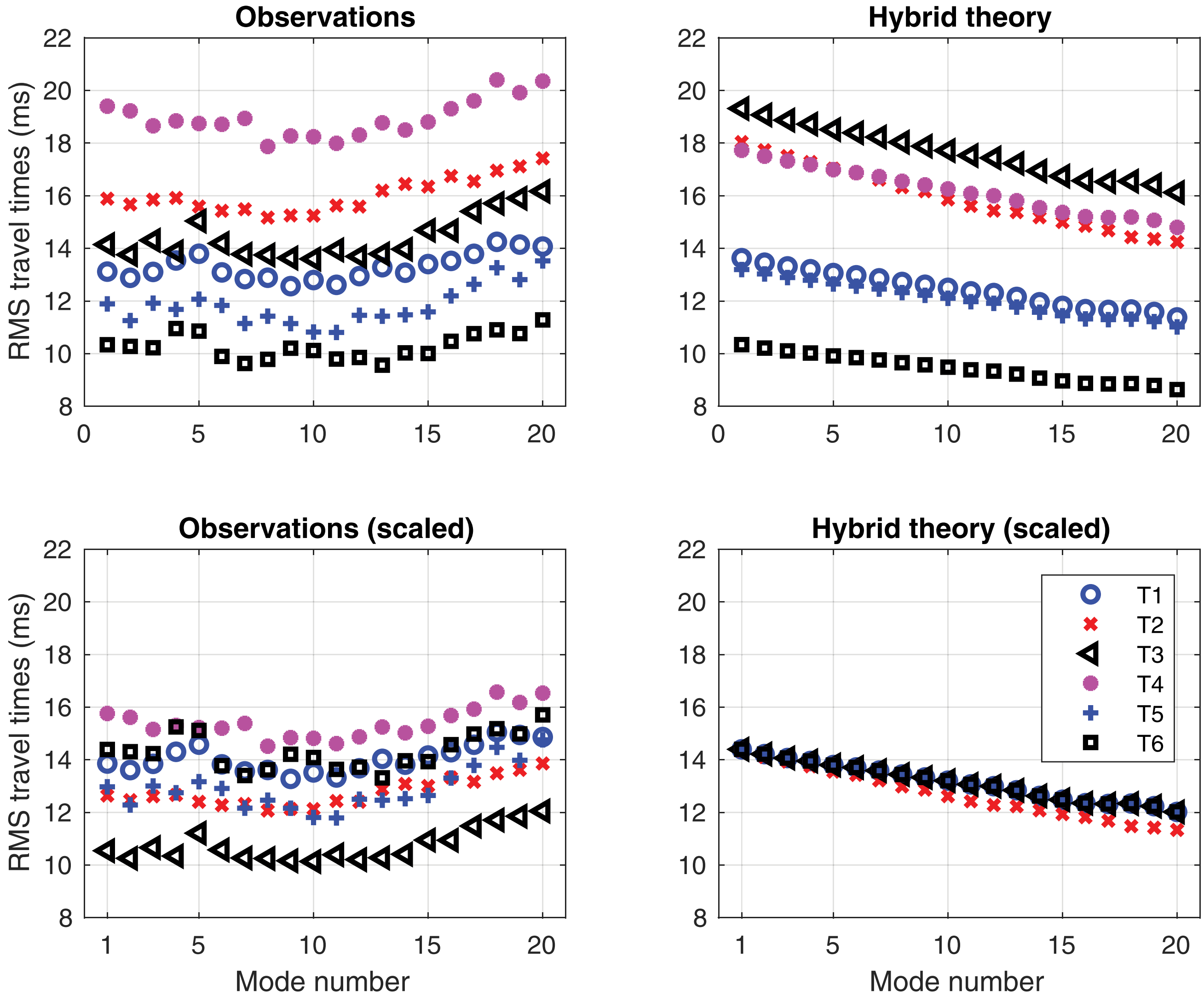

FIG. 14. (Color online) (Top) Travel-time variability due to internal waves from the PhilSea10 observations (left) and the hybrid predictions (right). (Bottom) observations and hybrid predictions scaled to a range of 250 km (range scaling of $\sqrt{R}$).

predictions plotted in the same figure. The no-internal-wave case shows only spreads due to frequency dispersion and finite bandwidth, but the hybrid mode predictions are wider due to travel-time wander. The predictions show a slight decrease in the mode time spreads with mode number. The observed time spreads used the monthly average intensities such as in Fig. 9. The observations show spreads comparable to the predictions and greater than the no-internal-wave case. The observations and the predictions both show an $R^{0.5}$ to $R^{0.6}$ increase in time spread across range for the low modes. The range scaling suggests that most of the mode time spread is due to the time wander which also varies as $\sqrt{R}$ across range. The observations, however, differ from the predictions in the following respects. While the hybrid theory predictions show a decrease in the time spread with mode number, the observations show a different trend. The discrepancy between the predictions and the observations is the most noticeable for modes 15–20. The hybrid theory performs poorly with respect to predicting the time spreads of the higher modes.

V. COMPARISONS TO OBSERVATIONS: INTENSITY STATISTICS

The narrowband intensities were calculated at the carrier frequencies (Table I). The average intensities were calculated for each month. There was not much monthly variation, nor any seasonal trend, in the monthly averages. Figure 16 shows the mean (normalized) of the intensities across months. The standard deviations of the monthly average intensities were around 0.5–0.7 dB. The normalized intensities for the different modes vary from −3 to +3 dB. Moving from the shortest (T6) to the longest (T3) range, the overall spread of values seems to decrease. For T6, the normalized intensity for mode 1 is +3 dB and for mode 20 is −3 dB. For T3, modes 1–20 are all around 0 dB. Figure 16 also shows the corresponding narrowband intensities from the transport theory predictions. The observations match the predictions.

The broadband intensities showed similar behavior. The mode arrivals at each range were time-aligned to compensate for internal tide and mesoscale-induced time wander.

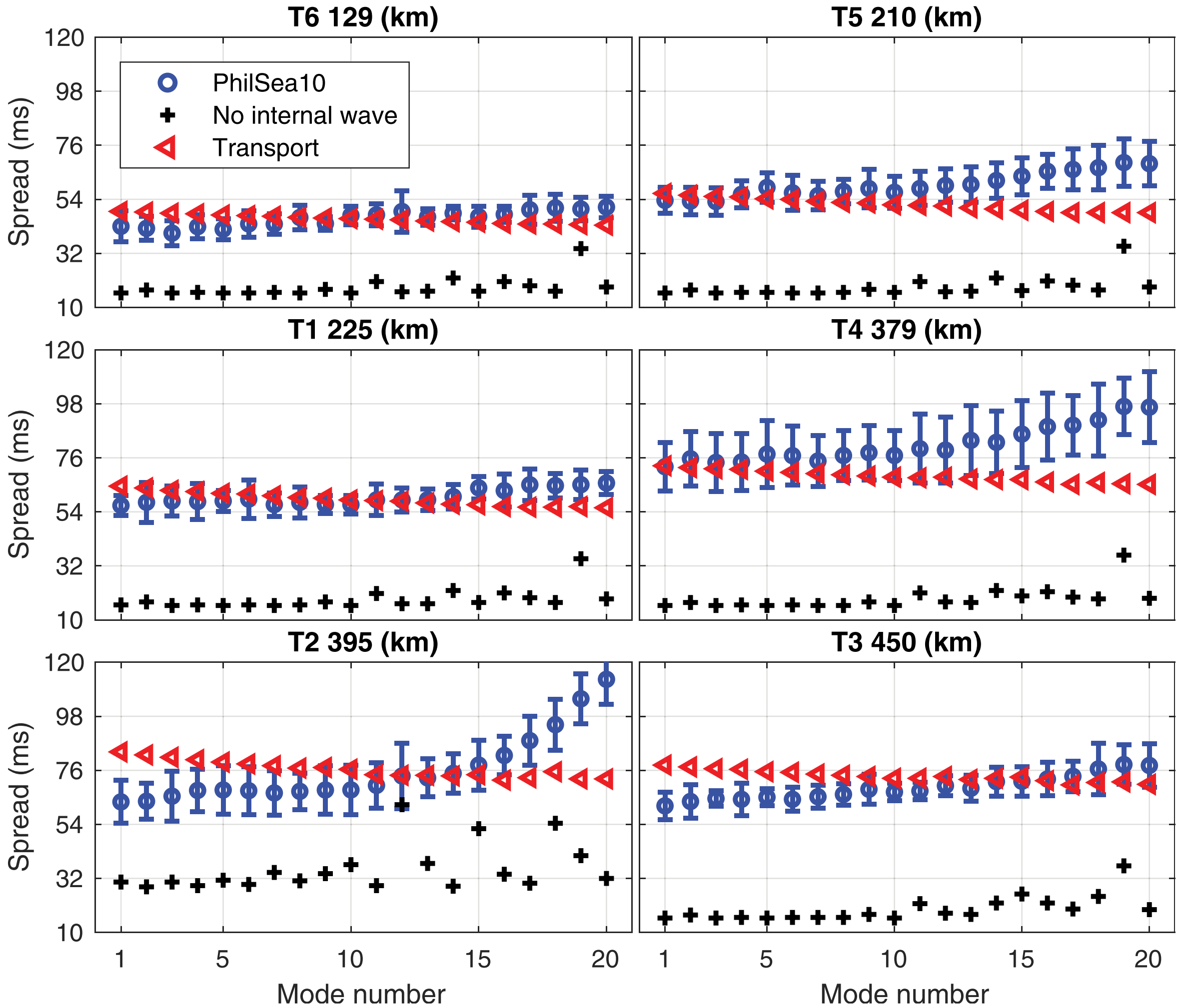

FIG. 15. (Color online) Time spread predictions and observations (with one standard deviation bars). There is no range scaling included in the plot.

The intensities of the time-aligned modes were averaged across transmissions and then normalized with the average over modes 1–20. Figure 9 shows the normalized intensities for the month of October 2010. Figure 17 shows the peak intensities of the pulses. The broadband peak intensities have a distribution similar to the narrowband intensities in Fig. 16. Progressing from the shortest range (T6) to the longest (T3), the broadband intensities show a spreading in energy across modes. Figure 17 also shows the intensity (peak) from the predictions. The predictions match the observations.

Taking the intensity analyses further, this work analyzed the histograms for the log-intensities (ι) and estimated the scintillation indices (SIs). The SI, which is closely related to kurtosis, is a measure of complex-Gaussianity in amplitude or Rayleigh distribution in intensity. The SI is defined as

$$SI = \frac{\langle I^2 \rangle}{\langle I \rangle^2} - 1. \tag{13}$$

For Rayleigh distributed random variables (I) with probability density function $P(I)$,

$$P(I) = \frac{1}{\langle I \rangle} e^{-I/\langle I \rangle}, \tag{14}$$

the value of $SI = 1$, and the standard deviation of the log-intensity $\sigma_\iota = 5.6\,dB$ (Dyer, 1970). For the log-normal distribution with Probability Density Function (PDF)

$$P(\iota) = N(0, \sigma_\iota^2), \tag{15}$$

the value of SI = 0.6. The observables SI and ι are complementary. The SI depends on the fourth order statistic of the intensity and hence weights the high intensities more than the low. The log-intensity ι, on the other hand, weights the low intensities. There are currently no analytic models for the variation of the mode SI across range. For narrowband modes, it is well known that the modes keep exchanging energy until they reach equipartition. At equipartition, the mode amplitudes are complex Gaussian random variables due to the central limit theorem (Colosi and Flatte, 1996; Dozier and Tappert, 1978a,b). For long range mode propagation, this causes the narrowband mode intensities to be Rayleigh distributed variables ($SI = 1$). This stage is called "full saturation." The modal path to full saturation across range and frequency is, however, not fully understood.

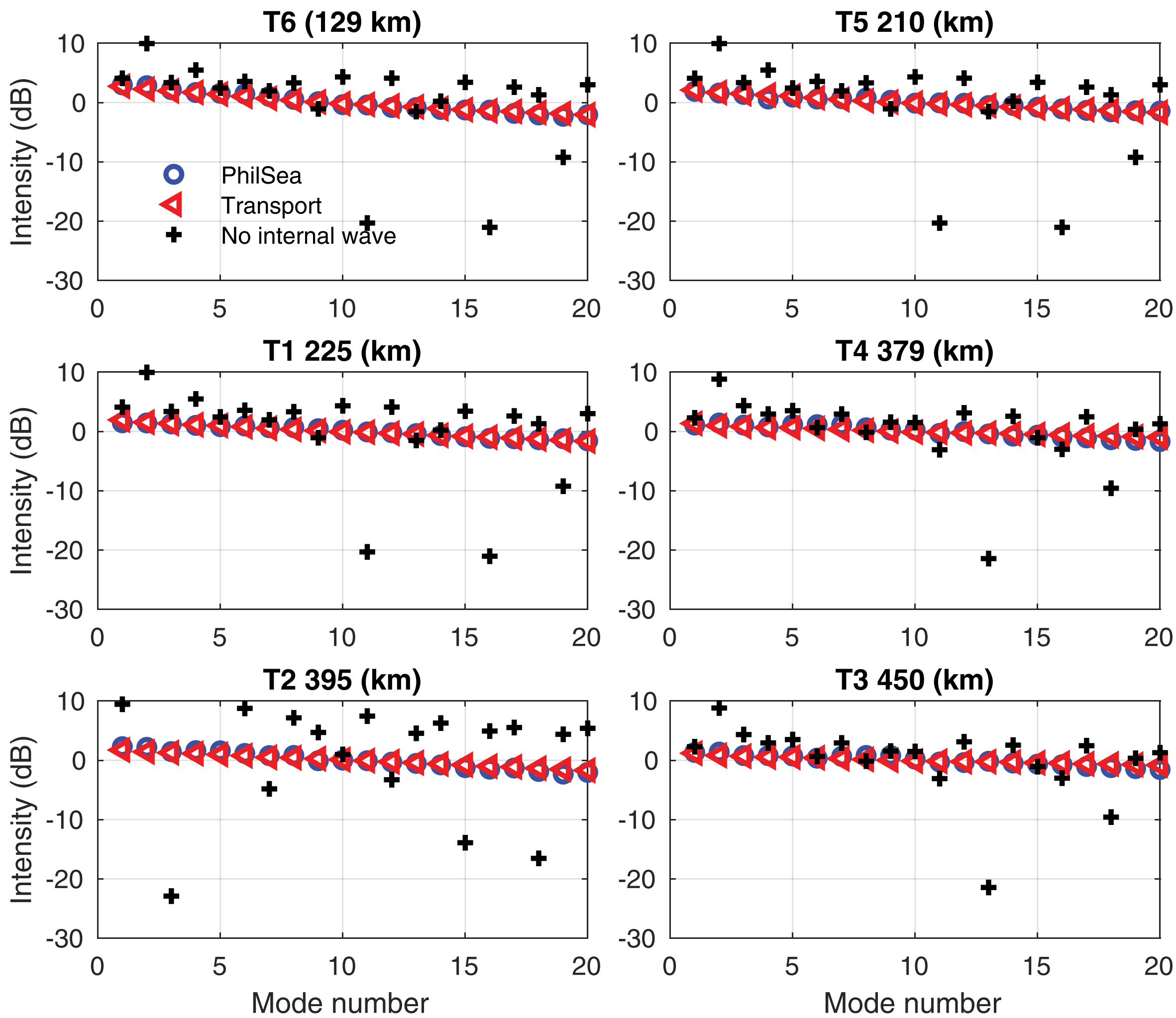

FIG. 16. (Color online) Intensity predictions and observations (narrowband). Similar to the previous plots the intensities are normalized (refer to the captions for Figs. 9 and 10).

Figures 18 shows the histograms of the narrowband intensities at different ranges. The figure also compares the histograms to the log-normal and Rayleigh density functions [Eqs. (15) and (14), respectively]. The histograms from the observations seem to follow the Rayleigh distribution at low intensities. This is, however, not true for the highest intensities of the observations. The variabilities in the log-intensity (σ_ι) and the SI [Eq. (13)] estimates are also indicated. The narrowband SI values are less than 1 for T6 and T5, equal to 1 for T1 and T2, and greater than 1 for T4 and T3. The narrowband log-intensities σ_ι are all around 5.6 dB. The source location T4 has $\sigma_\iota = 6.1$ dB, which is a little higher than the other source ranges. Figure 19 shows the distribution for the broadband intensities of the centroid. The broadband histograms have behaviors similar to the narrowband, with the low intensities matching the Rayleigh distribution, and the high intensities showing lower probabilities than the Rayleigh distribution. The σ_ι for the broadband intensities, however, stray far from the 5.6 dB values, which the narrowband statistics show. The broadband SI values are less than 1 for range T6, equal to 1 for T5, T1, and T2, and finally greater than 1 for T4 and T3.

VI. DISCUSSION AND CONCLUSION

There are two major results from the observations. The first is the extensive mode observations across a whole year in an oceanographically dynamic region. The mode observations allow comparison among the different source locations and ranges. The second is the comparison of the observations to the hybrid mode broadband model. The comparison among the different source ranges reveals the anisotropy and inhomogeneity in the oceanography across the PhilSea10 site. The model-data comparisons, on the other hand, suggest the limits of the hybrid transport theory approximation. The comparisons can be summarized as follows.

A. Comparisons across source ranges

Comparing the observations for the scaled travel-time fluctuations, T2 and T6 show the least mesoscale variability (Fig. 12). The highest mesoscale variabilities are for T1 and T4. This suggests that the paths to the north (T1) and southwest (T4) are subject to intense eddy fields that are potentially coherent across ranges greater than 200–300 km.

https://doi.org/10.1121/10.0000587

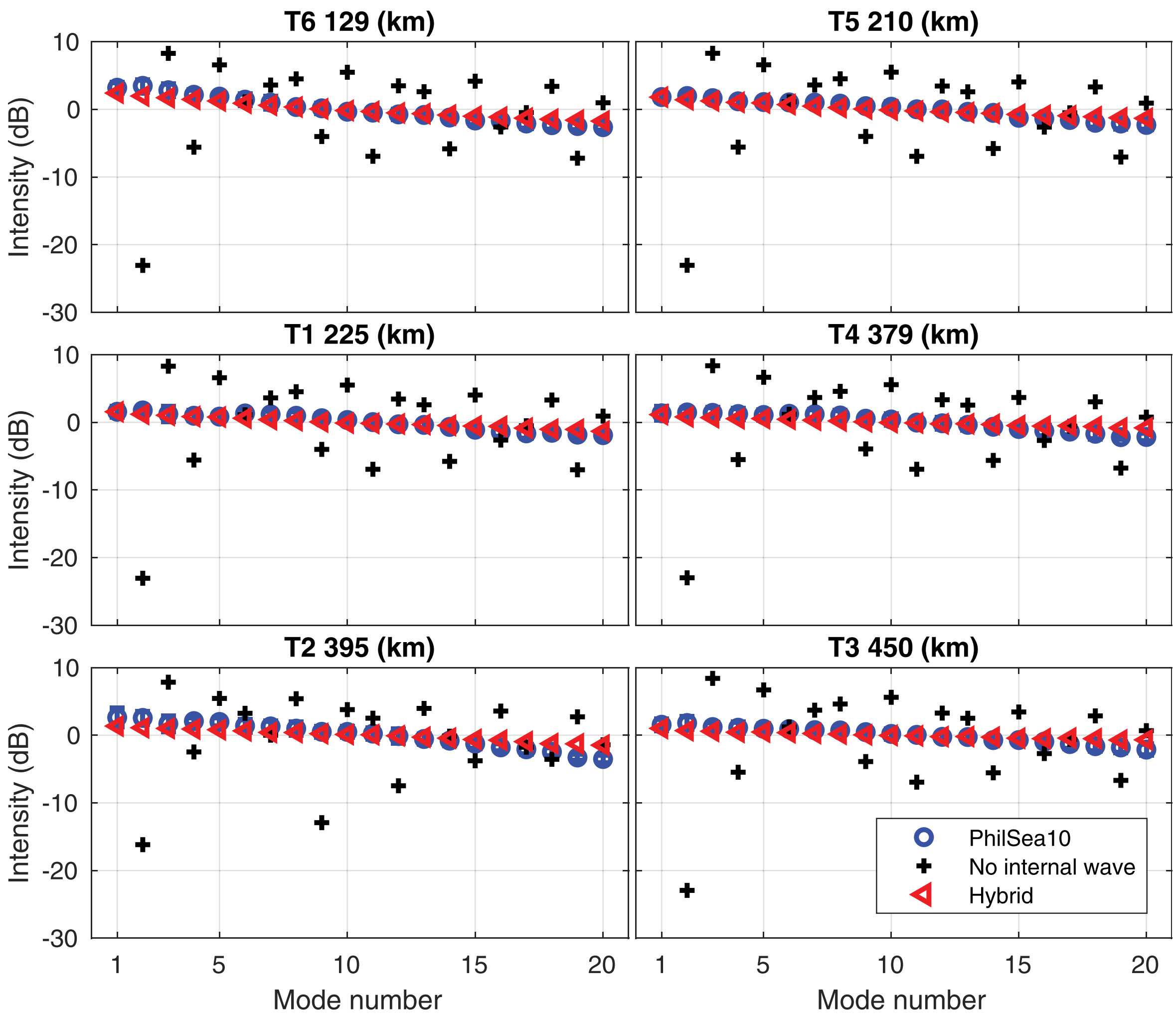

FIG. 17. (Color online) Intensity predictions and observations (broadband) based on normalized intensities. The peak broadband intensities for the no-internal-wave case and the hybrid theory were based on the predictions in Figs. 9. The peak intensities for the observations are the average of the monthly means similar to Fig. 9. The standard deviations of the monthly average intensities are 0.5–0.7 dB.

Satellite images for sea surface heights presented in Colosi *et al.* (2013b) showed eddy fields at the edges of the vertical line array (VLA) location and T1 during the month of May 2009. Ramp *et al.* (2017) reported that the northern source locations T1 and T5 are subject to intense eddy activity for depths of 280–360 m. The modes sample greater depths (Fig. 8) than the study in Ramp *et al.* (2017). The turning depths in Fig. 8 show that the low modes are most sensitive at depths of 1200–1750 m for 200–300 Hz and 1400–2000 m for 140–205 Hz. This suggests that for the mode turning depths the eddy fields are the most intense in the north and southwest. The Kuroshio Current that flows to the east of Taiwan and then heads north-west along the Ryuku Island arc is associated with intense eddies in the Philippine Sea (Qiu and Chen, 2010). Currently not much is known about the effect of the Kuroshio on eddy formation at the mode turning depths, to comment on the relationship of the current to the mode travel times.

Regarding the internal-tide-induced wander, Fig. 13 showed that there is significant variation between the different source locations and no clear range dependence. Oceanographic models and surface observations have suggested multiple internal tide generation sites (Sec. II). The acoustic variability across the different source ranges can be explained as follows. According to Eq. (7), the travel-time wander due to internal tides depends on both the wavelength and the orientation of the internal tide. Tides that have wavelengths much longer than the propagation distance or that propagate in a direction orthogonal to the acoustic path experience the most variability. Path ranges equal to or larger than the internal tide wavelengths would potentially average out the variability. The T6 range is only 129 km. Section III B mentioned that the internal tide mode 1 has wavelengths of 410 and 165 km for diurnal and semidiurnal frequencies, respectively. Due to the short T6 range, the modes see a significant amount of internal tide variability. T4, although being at a longer range than T6, shows significant internal-tide-induced travel-time variability. This is potentially due to the T4-DVLA path being orthogonal to significant internal tides coming from the southwest of the PhilSea10 site (Luzon Strait). In comparison, the source T2 that lies to the east has the least internal tide variability of

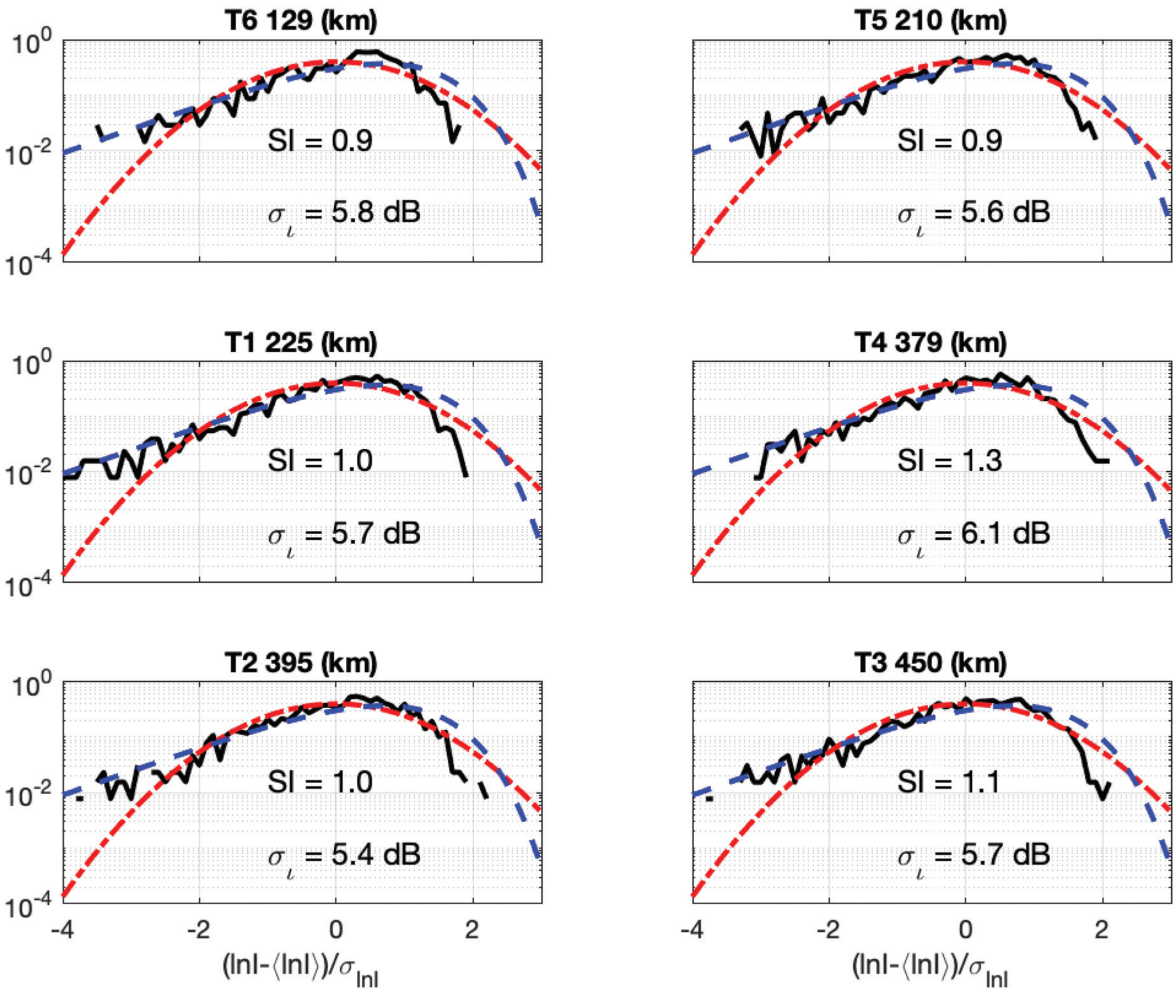

FIG. 18. (Color online) Histograms of narrowband intensities at the carrier frequencies (solid black line) with exponential PDF (blue dashed line) and log-normal PDF (red dashed-dotted line).

all the source ranges. The internal-tide-induced wander for T2 is 5 times less than that for T4. Comparing both the mesoscale and the tide variability across source ranges, T2 is the quietest and T4 the most dynamic. In contrast, the internal-wave-induced travel-time fluctuations in Fig. 14 do not show any such clear difference among source ranges. This suggests that the internal tide and mesoscale are highly anisotropic in the PhilSea10 region, whereas the internal wave field is not.

The fluctuations in mode intensities are due to both internal waves and also any changes in the background SSP. The intensity fluctuations due to internal waves cause scintillations that vary from one transmission to the next. The fluctuations due to changes in the background SSP, on the other hand, occur at monthly or seasonal time scales. The mode intensities did not reveal any monthly or seasonal variations but did show significant fluctuations due to internal waves (Figs. 18 and 19). Small intensity changes across months and seasons suggest that the background SSP remains fairly constant around the mode depths.

It is worth comparing the mode-based statistics in this paper with the statistics for the early "ray-like" arrivals from the same dataset reported by Colosi *et al.* (2019). The observations in Colosi *et al.* (2019) focused on intensity and travel time statistics (SI and σ_L) for early ray-like arrivals that had upper turning depths around 300–450 m. The rays for the different source ranges were either in the unsaturated or the partially saturated regime ($SI < 1$ or $SI > 1$). The rays first go from the unsaturated ($SI < 1$) to the partially saturated regime ($SI > 1$) and then finally settle into full saturation (Flatte, 1983). This behavior can be explained using a kinematic model (Colosi and Baggeroer, 2004). Figures 18 and 19 show the mode intensity distributions. Consider the progression of mode SI values for source ranges T6 (129 km), T5 (210 km), T1 (225 km), T4 (379 km), and T3 (450 km), which occupy roughly the same frequency band. The SIs start from a value less than 1, then become equal to 1, after which they exceed 1, and finally tend back towards 1. This suggests that the mode intensity distributions across range are transitioning from unsaturated to partially saturated, and then finally approaching full saturation.

For travel-time fluctuations, Colosi *et al.* (2019) estimated the travel-time wander in the mesoscale, internal tide, and internal wave frequency bands. The travel-time

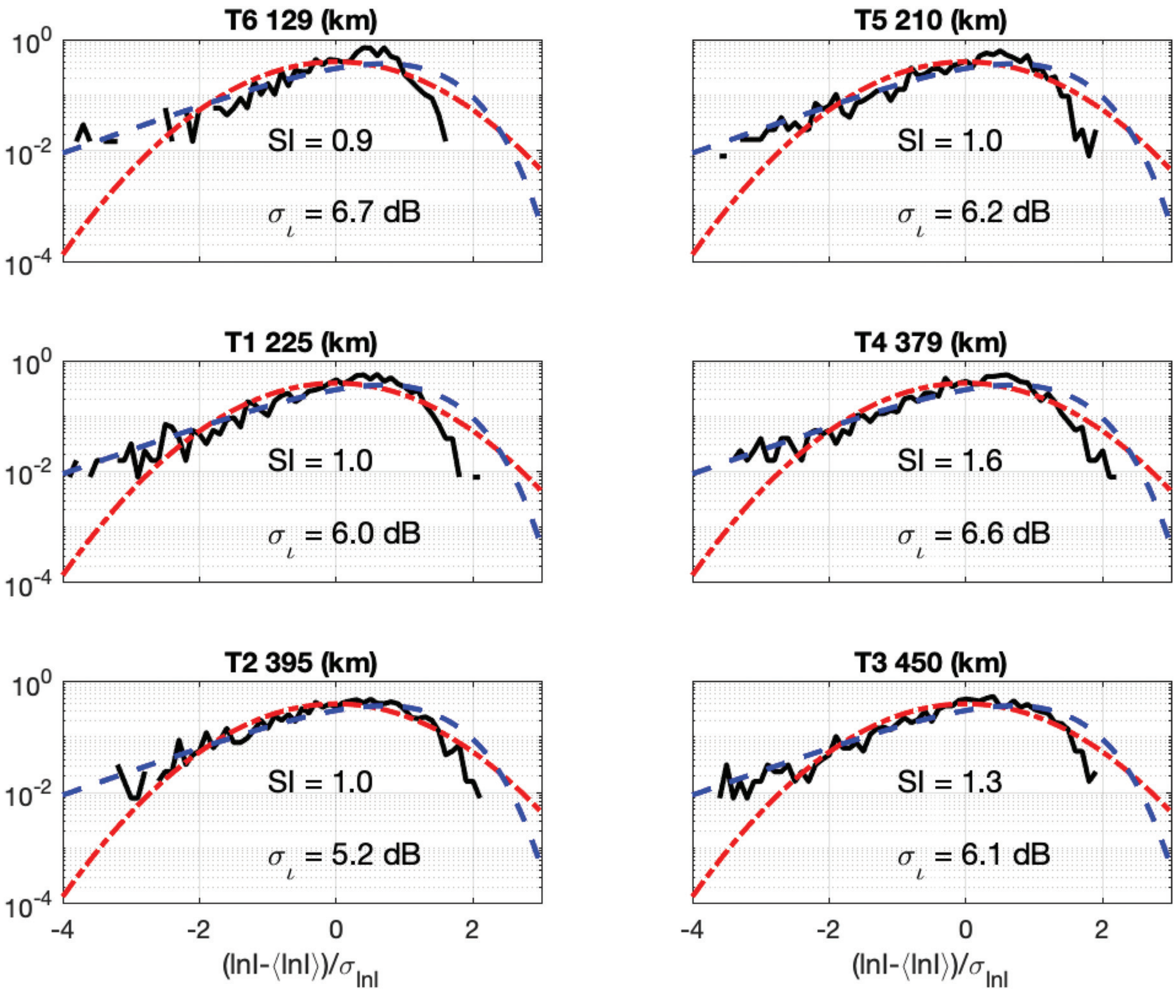

FIG. 19. (Color online) Histograms of broadband intensities (solid black line) with exponential PDF (blue dashed line), and log-normal PDF (red dashed-dotted line).

fluctuations of the ray arrivals for the internal tide and mesoscale bands are on the order of several 10 s of milliseconds, which is similar to the mode observations reported in the same bands. For internal tides, the ray-like arrivals showed a similar anisotropy as the modes, with the highest variability for T2 and T4. The internal-wave-induced travel-time wander for the ray measurements, is, however, less than the mode observations. This is due to the differences in the nature of low-mode propagation vs steep rays with respect to the "mode launch-angle" and the range-depth structure of the internal wave spectrum (Colosi, 2016). The modes can be approximated by rays with shallow launch angles, which sample the internal wave field for longer range segments than the steep rays. The low modes hence suffer higher amounts of internal-wave-induced travel-time wander than the steep rays.

B. How well does the hybrid model work?

The model-data comparisons show that the predictions work well for mode intensities (Figs. 16 and 17). Transport theory thus seems to be robust for predicting peak intensity levels for broadband pulses and narrowband intensities. For travel-time variability, Fig. 14 shows that the hybrid predictions and the observations for modes 1–10 agree within a factor of 1.5. The fluctuations for the high modes (10–20) are, however, greater than the predictions, suggesting the limitations of the hybrid theory. The hybrid model relies on the adiabatic approximation to obtain the cross-frequency phase coherence. This approximation works well when the different frequencies have the same turning depths. Figure 8 showed that the spread of turning depths increases with mode number. The higher modes are, thus, not a good fit for the adiabatic phase coherence model. For the mean pulse intensity predictions, the model matches the main arrivals, and yet does not fully model the low intensity arrival in the sidelobes (Fig. 9). The mode time-spread predictions with 10 dB cutoff, however, work well for the low modes (1–10) and not so well for the high modes (15–20) (Fig. 15). This again suggests that the hybrid model is less accurate for the modes that have a wide spread in turning depths.

Section IV reported that the time spread observations showed an $R^{0.5}$ to $R^{0.6}$ dependence, which is less than the $R^{3/2}$ dependence predicted by Udovydchenkov and Brown (2008). The discrepancy could have several causes. The first is that the $R^{3/2}$ prediction is for high mode numbers, and the

https://doi.org/10.1121/10.0000587

results in this paper are for the lowest modes. The second is that the predictions by Udovydchenkov and Brown (2008) and Udovydchenkov *et al.* (2012) were made in the context of the Long Range Ocean Acoustic Propagation EXperiment (LOAPEX) (Mercer *et al.*, 2009), which was conducted in the North Pacific and used much lower frequencies around 75 Hz. Calculations showed that waveguide-induced dispersion is greater for the LOAPEX environment than the Philippine Sea. The third is that the predictions by Udovydchenkov and Brown (2008) and Udovydchenkov *et al.* (2012) use the physics of the action variable, which is a ray-based construct, and then a WKB approximation to the modes. This work, on the other hand, exclusively uses modes and incorporates the coupling physics. The results in this paper do not imply, however, that the $R^{0.5}$ dependence stays uniform across range. The $R^{0.5}$ dependence mostly comes from the adiabatic approximation that the hybrid theory uses. At ranges much greater than those in PhilSea10, the coupling-induced dispersion may cause the spreads to increase at a faster rate than $R^{0.5}$. The spreading is also complicated at ranges less than those in PhilSea10. Close to the source, the distribution of energies across modes is still in a state of flux (Fig. 10) with the mode pulses not fully formed. The mode pulses can, thus, vary significantly across short distances. This can potentially lead to a non-uniform range dependence of time spreads for ranges much shorter than PhilSea10.

ACKNOWLEDGMENTS

The work of T.K.C. was supported by the Office of Naval Research Global and the Naval Research Board India. This material is based in part upon work supported by the U.S. Office of Naval Research Ocean Acoustics and Undersea Signal Processing programs. Any opinions, findings, and conclusions or recommendations expressed in this publication are those of the authors and do not necessarily reflect the views of the Office of Naval Research.

APPENDIX: MODE SPATIAL FILTERING DETAILS

Estimating the mode amplitudes a_m from the received pressure field on a vertical array is a spatial filtering problem. The mode estimate $\hat{\mathbf{a}}$ is obtained by projecting the received pressure field (at each frequency) onto the mode spatial filter. This article uses the "matched mode filter" by Ferris (1972) and Ingenito (1973). The matched filter beamformer is given by

$$\hat{\mathbf{W}}^{mf} = Y, \qquad \text{(A1)}$$

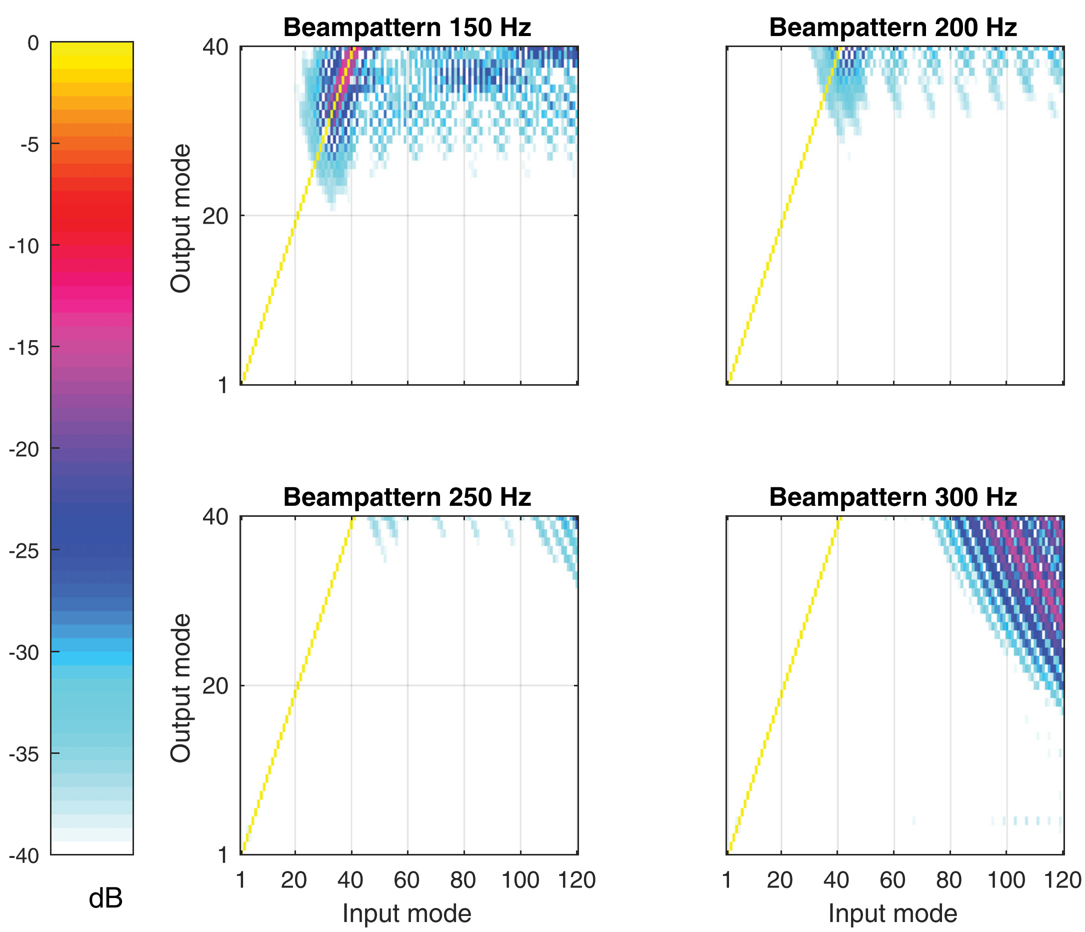

FIG. 20. (Color online) Matched filter beam pattern calculated from the normalized cross-correlation matrix [Eq. (A2)] of the mode shapes (from Fig. 5) as sampled at the vertical array.

where $\boldsymbol{\Psi}$ is a matrix of the mode shapes sampled at the array. Figure 20 shows the "beampattern" for the sample mode shapes beamformer (Wage, 2000; Wage *et al.*, 2003). The beampattern calculated with the normalized cross-correlation of the sampled mode shapes (Fig. 5) is given by

$$B(m,n) = 20\log_{10}\left(\frac{|\boldsymbol{\Psi}_m^H \boldsymbol{\Psi}_n|}{||\boldsymbol{\Psi}_m||||\boldsymbol{\Psi}_n||}\right). \quad \text{(A2)}$$

A perfectly diagonal beampattern would imply that the input mode will be observed at the output of the beamformer sans interference. However, the beampatterns in Fig. 20 are only diagonal for modes $\approx$ 1–20 (at 150 Hz), 1–30 (at 200 Hz), and 1–35 (at 250 and 300 Hz). For higher modes, there are significant cross-diagonal terms, which implies cross-modal interference. Source T2 used frequencies 140–205 Hz and the other sources used approximately used 200–300 Hz. In order to keep the analysis uniform for all source frequencies, this paper restricted the analysis only to the first 20 modes.

The sampled mode shapes vary as a function of time due to the changes in the sound-speed profile at the receiving array due to internal waves, internal tides, and mesoscale variations. To minimize the mismatch, the mode shapes at the array were calculated based on the *in situ* environmental measurements made during PhilSea10. The sound-speed profile calculations require both temperature (T) and salinity (S) profiles. For the T-profile, the calculations used the thermistor measurements at the hydrophone depths (Fig. 4). For salinity values, there were, unfortunately, no moored measurements at the array that lasted the whole experiment. To estimate the S profile, a T–S curve was estimated from the ship CTD casts (Fig. 1). The temperature profiles were mapped onto the T–S curve to estimate the salinities. In order to reduce mismatch over time, calculations showed that 15 days is a good estimate for the coherence time for the mode (1–20) shapes. The mode shapes were thus calculated in 15 days blocks and used to beamform for the modes. For each source, a 0.5 s time window was chosen for the broadband mode processor (Wage *et al.*, 2003). Table II indicates the windows that were chosen.

Figure 6 shows the mode results for the PhilSea10 arrivals in Fig. 3. The modes 1, 10, and 20 arrive approximately at the same time. This is similar to the predictions in Fig. 7. The mode 20 results at T6 show some minor arrivals down 15–20 dB that are actually aliased arrivals from modes greater than 100. For the other ranges, mode 20 shows a wider time spread than modes 1 and 10. The wider time spread is due to internal-wave-induced coupling from the other high modes. Similar processing was implemented for all the other PhilSea10 receptions.

TABLE II. Time windows chosen for PhilSea10 broadband mode processing.

Source	Frequencies (Hz)	Time limit (s)
T1	200–300	151.5–152
T2	140–205	267–267.5
T3	225–325	303.5–304
T4	225–325	255.6–256.1
T5	205–305	141.5–142
T6	200–300	87.0–87.5

[1]Other PhilSea analysis papers (Andrew *et al.*, 2016; White *et al.*, 2013) have used the Thermodynamic Equation of Seawater (TEOS-10) toolbox (IOC *et al.*, 2010). Comparisons between the TEOS-10 and Del Grosso methods showed that the sound speed estimates using the two methods were almost the same (<0.08 m/s).

Andrew, R. K., Ganse, A., White, A. W., Mercer, J. A., Dzieciuch, M. A., Worcester, P. F., and Colosi, J. A. (**2016**). "Low-frequency pulse propagation over 510 km in the Philippine sea: A comparison of observed and theoretical pulse spreading," J. Acoust. Soc. Am. **140**(1), 216–228.

Chandrayadula, T. K., Colosi, J. A., Worcester, P. F., Dzieciuch, M. A., Mercer, J. A., Andrew, R. K., and Howe, B. M. (**2013a**). "Observations and transport theory analysis of low frequency, acoustic mode propagation in the eastern North Pacific Ocean," J. Acoust. Soc. Am. **134**(4), 3144–3160.

Chandrayadula, T. K., Wage, K. E., Worcester, P. F., Dzieciuch, M. A., Mercer, J. A., Andrew, R. K., and Howe, B. M. (**2013b**). "Reduced rank models for travel time estimation of low order mode pulses," J. Acoust. Soc. Am. **134**(4), 3332–3346.

Colosi, J. A. (**2016**). *Sound Propagation Through the Stochastic Ocean* (Cambridge University Press, Cambridge, UK), Chap. 8, pp. 333–402.

Colosi, J. A., and Baggeroer, A. B. (**2004**). "On the kinematics of broadband multipath scintillation and the approach to saturation," J. Acoust. Soc. Am. **116**(6), 3515–3522.

Colosi, J. A., and Brown, M. G. (**1998**). "Efficient numerical simulation of stochastic internal-wave-induced sound-speed perturbation fields," J. Acoust. Soc. Am. **103**(4), 2232–2235.

Colosi, J. A., Chandrayadula, T. K., Voronovich, A. G., and Ostashev, V. E. (**2013a**). "Coupled mode theory for sound transmission through an ocean with random sound speed perturbations: Coherence in deep water environments," J. Acoust. Soc. Am. **134**(4), 3119–3133.

Colosi, J. A., Cornuelle, B. D., Worcester, P. F., Dzieciuch, M. A., and Chandrayadula, T. K. (**2019**). "Observations of phase and intensity fluctuations on a large aperture vertical array for 6 acoustic paths in the Philippine Sea and comparisons to Feynman path integral theory," J. Acoust. Soc. Am. **146**(1), 567–585.

Colosi, J. A., and Flatte, S. M. (**1996**). "Mode coupling by internal waves for multimegameter acoustic propagation in the ocean," J. Acoust. Soc. Am. **100**(6), 3607–3620.

Colosi, J. A., and Morozov, A. K. (**2009**). "Statistics of normal mode amplitudes in an ocean with random sound-speed perturbations: Cross-mode coherence and mean intensity," J. Acoust. Soc. Am. **126**(3), 1026–1035.

Colosi, J. A., Van Uffelen, L. J., Cornuelle, B. D., Dzieciuch, M. A., Worcester, P. F., Dushaw, B. D., and Ramp, S. R. (**2013b**). "Observations of sound-speed fluctuations in the western Philippine Sea in the spring of 2009," J. Acoust. Soc. Am. **134**(4), 3185–3200.

Del Grosso, V. A. (**1974**). "New equation for the speed of sound in natural waters (with comparison to other equations)," J. Acoust. Soc. Am. **56**(4), 1084–1091.

Dozier, L., and Tappert, F. (**1978a**). "Statistics of normal mode amplitudes in a random ocean. 1. Theory," J. Acoust. Soc. Am. **63**(2), 353–365.

Dozier, L., and Tappert, F. (**1978b**). "Statistics of normal mode amplitudes in a random ocean. 2. Computations," J. Acoust. Soc. Am. **64**(2), 533–547.

Dushaw, B. D. (**2003**). "Mapping and wavenumber resolution of line-integral data for observations of low-mode internal tides," J. Atmos. Ocean. Tech. **20**, 1043–1059.

Dyer, I. (**1970**). "Statistics of sound propagation in the ocean," J. Acoust. Soc. Am. **48**, 337–345.

Ferris, R. H. (**1972**). "Comparison of measured and calculated normal-mode amplitude functions for acoustic waves in shallow water," J. Acoust. Soc. Am. **52**(3), 981–988.

Flatte, S. (**1983**). "Wave propagation through random media: Contributions from Ocean Acoustics," Proc. IEEE **71**(11), 1267–1294.

Garrett, C., and Munk, W. (**1972**). “Space-time scales of internal waves,” J. Geophys. Res. **3**, 225–264, https://doi.org/10.1080/03091927208236082.

Garrett, C., and Munk, W. (**1975**). “Space-time scales of internal waves: A progress report,” J. Geophys. Res. **80**, 291–297, https://doi.org/10.1029/JC080i003p00291.

Ingenito, F. (**1973**). “Measurements of mode attenuation coefficients in shallow water,” J. Acoust. Soc. Am. **53**(3), 858–863.

IOC, SCOR, and IAPSO (**2010**). “The international thermodynamic equation of seawater—2010: Calculation and use of thermodynamic properties, Intergovernmental Oceanographic Commission, Manuals and Guides No 56, UNESCO (English),” http://www.teos-10.org (Last viewed October 28, 2019).

Jensen, F. B., Kuperman, W. A., Porter, M. B., and Schmidt, H. (**1994**). *Computational Ocean Acoustics* (American Institute of Physics, Melville, NY), Chap. 5, pp. 257–322.

Kerry, C. G., Powell, B. S., and Carter, G. S. (**2013**). “Effects of remote generation sites on model estimates of M_2 internal tides in the Philippine Sea,” J. Phys. Oceanogr. **43**, 187.

Locarnini, R. A., Mishonov, A. V., Antonov, J. I., Boyer, T. P., Garcia, H. E., Baranova, O. K., Zweng, M. M., Paver, C. R., Reagan, J. R., Johnson, D. R., Hamilton, M., and Seidov, D. (**2018a**). *World Ocean Atlas 2013 Volume 1: Temperature* (NOAA Atlas NESDIS).

Locarnini, R. A., Mishonov, A. V., Baranova, O. K., Boyer, T. P., Zweng, M. M., Garcia, H. E., Reagan, J. R., Seidov, D., Weathers, K., Paver, C. R., and Smolyar, I. (**2018b**). *World Ocean Atlas 2018 Volume 2: Salinity* (NOAA Atlas NESDIS).

Mercer, J. A., Colosi, J. A., Howe, B. M., Dzieciuch, M. A., Stephen, R., and Worcester, P. F. (**2009**). “LOAPEX: The long-range ocean acoustic propagation experiment,” IEEE. J. Ocean. Eng **34**(1), 1–11.

Morozov, A. K., Webb, D. C., Ching-Sang, Chiu, Worcester, P. F., Dzieciuch, M. A., Sagen, H., Guigné, J. Y., and Altshuler, T. W. (**2016**). “High-efficient tunable sound sources for ocean and bottom tomography, 15 years of operating history,” in *Proceedings of OCEANS 2016 MTS/IEEE*, September 19–23, Monterey, CA, pp. 1–10.

Niwa, Y., and Hibiya, T. (**2004**). “Three-dimensional numerical simulation of M_2 internal tides in the East China Sea,” J. Geophys. Res. **109**, C04027, https://doi.org/10.1029/2003JC001923.

Porter, M. B. (**2001**). *The Kraken Normal Mode Program* (SACLANT Undersea Research Centre, La Spezia, Italy).

Qiu, B. (**1999**). “Seasonal eddy field modulation of the North Pacific Subtropical Countercurrent: TOPEX/Poseidon observations and theory,” J. Phys. Oceanogr. **29**, 2471–2486.

Qiu, B., and Chen, S. (**2010**). “Interannual variability of the North Pacific subtropical countercurrent and its associated mesoscale eddy field,” J. Phys. Oceanogr. **40**, 213–225.

Raghukumar, K., and Colosi, J. A. (**2014**). “High frequency normal mode statistics in a shallow water waveguide: The effect of random linear internal waves,” J. Acoust. Soc. Am. **136**, 66–79.

Ramp, S., Colosi, J., Worcester, P., Bahr, F., Heaney, K., Mercer, J., and Van Uffelen, L. (**2017**). “Eddy properties in the subtropical countercurrent, Western Philippine Sea,” Deep Sea Res. Part I Oceanogr. Res. Papers **125**, 11–25.

Shang, E. (**1989**). “Ocean acoustic tomography based on adiabatic mode theory,” J. Acoust. Soc. Am. **85**(4), 1531–1537.

Udovydchenkov, I. A., and Brown, M. G. (**2008**). “Modal group time spreads in weakly range-dependent deep ocean environment,” J. Acoust. Soc. Am. **123**(1), 41–50.

Udovydchenkov, I. A., Brown, M. G., Duda, T. F., Mercer, J. A., Andrew, R. K., Worcester, P. F., Dzieciuch, M. A., Howe, B. M., and Colosi, J. A. (**2012**). “Modal analysis of the range evolution of broadband wavefields in the North Pacific Ocean: Low mode numbers,” J. Acoust. Soc. Am. **131**(6), 4409–4427.

Van Kampen, N. G. (**2007**). *Stochastic Processes in Physics and Chemistry*, 3rd ed. (Elsevier, Amsterdam, the Netherlands), Chap. 11, pp. 275–356.

Wage, K. E. (**2000**). “Broadband modal coherence and beamforming at megameter ranges,” Ph.D. thesis, MIT/WHOI, Cambridge, MA.

Wage, K. E., Baggeroer, A. B., and Preisig, J. C. (**2003**). “Modal analysis of broadband acoustic receptions at 3515-km range in the North Pacific using short-time Fourier techniques,” J. Acoust. Soc. Am. **113**(2), 801–817.

White, A. W., Andrew, R. K., Mercer, J. A., Worcester, P. F., Dzieciuch, M. A., and Colosi, J. A. (**2013**). “Wavefront intensity statistics for 284-Hz broadband transmissions to 107-km range in the Philippine sea: Observations and modeling,” J. Acoust. Soc. Am. **134**(4), 3347–3358.

Worcester, P. F., Cornuelle, B. D., Dzieciuch, M. A., Munk, W. H., Howe, B. M., Mercer, J. A., Spindel, R. C., Colosi, J. A., Metzger, K., Birdsall, T. G., and Baggeroer, A. B. (**1999**). “A test of basin-scale acoustic thermometry using a large-aperture vertical array at 3250-km range in the eastern North Pacific Ocean,” J. Acoust. Soc. Am. **105**(6), 3185–3201.

Worcester, P. F., Dzieciuch, M. A., Mercer, J. A., Andrew, R. K., Dushaw, B. D., Baggeroer, A. B., Heaney, K. D., D’Spain, G. L., Colosi, J. A., Stephen, R. A., Kemp, J. N., Howe, B. M., Van Uffelen, L. J., and Wage, K. E. (**2013**). “The North Pacific Acoustic Laboratory deep-water acoustic propagation experiments in the Philippine Sea,” J. Acoust. Soc. Am. **134**, 3359–3375.

Worcester, P. F., and Spindel, R. C. (**2005**). “North Pacific acoustic laboratory,” J. Acoust. Soc. Am. **117**(3), 1499–1510.